Materials & Design 260 (2025) 115219

Contents lists available at ScienceDirect

Materials & Design

journal homepage: www.elsevier.com/locate/matdes

# Identification of the role of zinc in Sn–Cu solder and interfacial intermetallic growth through experimental results and phase-field simulations

H.R. Kotadia [a,b,*], A. Rahnama [b], F. Tang [b], J.I. Ahuir-Torres [a], G. West [b], A. Das [c], S.H. Mannan [d]

[a] School of Engineering, Liverpool John Moores University, Liverpool L3 3AF, UK
[b] WMG, the University of Warwick, Coventry CV4 7AL, UK
[c] Faculty of Science and Engineering, Swansea University Bay Campus, Fabian Way, Swansea SA1 8EN, UK
[d] Department of Physics, King's College London, Strand, London WC2R 2LS, UK

ARTICLE INFO

*Keywords:*
Sn-Cu solder
Pb-free solder
Intermetallic compounds (IMCs)
Solidification
Phase-field simulations

ABSTRACT

Intermetallic compound (IMC) formation significantly impacts the reliability of lead-free solder joints, with trace elements like Ni and Zn offering potential to control IMC growth. However, the mechanisms by which trace Zn influences microstructural evolution and interfacial reactions remain underexplored. This study examines microstructural evolution and interfacial behaviour in five Sn–Cu–Zn solder alloys (0–1 wt% Zn). Zn destabilises the eutectic interface, producing cellular morphologies with mixed eutectic at cell centres and CuZn IMCs in interdendritic regions. Even trace Zn notably affects solidification by reducing undercooling and altering β-Sn growth. While trace Zn has limited effect on suppressing η-$Cu_6Sn_5$, ε-$Cu_3Sn$, or Kirkendall voids on Cu, it reduces IMC thickness, indicating growth inhibition. Adding $\geq$ 0.8 wt% Zn reduces IMC thickness at 150 °C by 68.5 % after 1000 h, from ~ 16.5 μm (Sn–Cu) to ~ 5–5.5 μm, also lowering void growth. The presence of a thin γ-$Cu_5Zn_8$ layer (<100 nm) at the interface substantially alters the nucleation, growth, and morphology of the η-phase. Phase-field simulation helped explain the experimental observations indicating thin γ-$Cu_5Zn_8$ formation at the solder-substrate interface that enhanced nucleation of η-$Cu_6Sn_5$ but reduced the growth kinetics of η and ε phases by creating a diffusion barrier for Cu atoms.

## 1. Introduction

The push to eliminate lead (Pb) in consumer electronics has driven significant advancements in lead-free solder technology over the past two decades. Traditional Sn–37Pb solder, widely used for its excellent soldering properties, was phased out due to environmental and health concerns, as mandated by global regulatory frameworks such as the Restriction of Hazardous Substances (RoHS) directive [1–5]. Among the proposed alternatives, eutectic Sn–Cu solder (Sn–0.7 wt% Cu) has emerged as a strong candidate, particularly for wave soldering applications. Its wide adoption is attributed to its excellent solderability in industrial-scale production and its cost-effectiveness compared to Ag-containing alloys, such as Sn–Ag and Sn–Ag–Cu (SAC) systems [6].

Despite its advantages, the Sn–Cu solder alloy poses significant challenges compared to traditional Sn–Pb solder. Issues such as the formation of Kirkendall voids [7–10], difficulty in nucleating the primary β-Sn phase [11], accelerated intermetallic compound (IMC) growth [2], and the spalling of interfacial IMCs [12,13] are particularly pronounced in high-temperature applications exceeding 125 °C. These limitations underscore the need for an in-depth understanding of the alloy's solidification behaviour and microstructural evolution to improve its performance and reliability. Extensive research has been devoted to characterising the solidification processes in Sn–Cu alloys, focusing on the nucleation and growth of primary β-Sn and the eutectic β-Sn + η-$Cu_6Sn_5$ phases [14]. The eutectic reaction, L → β-Sn + η-$Cu_6Sn_5$, dominates the Sn–Cu system and plays a crucial role in determining the alloy's microstructure and mechanical properties. To mitigate some of the inherent drawbacks of the Sn–Cu eutectic, researchers have explored the addition of trace elements such as Pb, Ag, Bi, Ni, and Zn [15–19]. These studies reveal that trace element additions

* Corresponding author at: School of Engineering, Liverpool John Moores University, Liverpool L3 3AF, UK.
*E-mail addresses:* h.r.kotadia@ljmu.ac.uk (H.R. Kotadia), samjid.mannan@kcl.ac.uk (S.H. Mannan).

https://doi.org/10.1016/j.matdes.2025.115219
Received 27 May 2025; Received in revised form 14 November 2025; Accepted 24 November 2025
Available online 29 November 2025

can destabilise the eutectic interface, leading to cellular eutectic structures and modifying microstructural features.

Besides the bulk solidification behaviour of the solder, the interfacial reactions at the solder/substrate interface play a crucial role in ensuring the reliability and mechanical integrity of solder joints [20,21]. The nucleation and growth of IMCs at this interface are critical factors that influence the performance of microelectronic packages. In the case of Sn-based solders on Cu substrates, two primary IMCs, $Cu_6Sn_5$ (η phase) and $Cu_3Sn$ (ε phase), are known to nucleate heterogeneously during soldering [22]. These IMCs form within milliseconds during the early stages of reflow and quickly develop into continuous layers. The thickness, morphology, and crystallography of these interfacial Cu–Sn IMCs significantly affect solder joint reliability [23,24]. Notably, the hexagonal η-phase (space group $P6_3/mmc$) transitions to its monoclinic η'-phase (space group C2/c) at 186 °C, generating internal stresses in the solder joint that compromise its mechanical performance [24,25]. Studies have suggested that stabilising the η-phase over a broad temperature range could improve joint strength and durability [26]. Trace additions of elements such as Au, Ni, and Zn have been shown to stabilise the η-phase from –80 °C to 240 °C, over extended periods, preventing its transformation to η'-phase [27–30].

In addition to stabilising the η-phase, specific trace elements can suppress the formation of the ε-phase, thereby mitigating the formation of Kirkendall voids and enhancing joint reliability [31–33]. For instance, Al, Ag, Bi, Cr, In, Ni, and Zn have been shown to influence interfacial IMC formation and bulk solder microstructure through mechanisms such as solute segregation, diffusion barrier formation, and altered thermodynamic stability [12,34–38]. Ni and Zn, in particular, exhibit high solubility in the η-phase and effectively alter interfacial reaction kinetics, often leading to refined and more stable microstructures. Ni additions typically result in the formation of $(Cu,Ni)_6Sn_5$ and suppress ε-IMC growth [39], while Ag refines the eutectic microstructure and enhances creep resistance in Sn-based solder [40,41]. Trace Zn additions have been reported to enhance shear strength and reduce crack propagation by refining the IMC morphology and limiting the growth of brittle phases at the solder/Cu interface [42]. Bi and In are known to improve wetting and reduce undercooling [43], and Al has been reported to form thermally stable IMCs that can act as diffusion barriers, thereby contributing to reduced IMC layer growth and enhanced joint reliability [8]. However, excessive concentrations of these elements may lead to the formation of undesirable secondary IMCs, which can negatively impact mechanical and thermal performance [12,34]. Despite these advances, the underlying mechanisms governing the suppression and modification of interfacial IMCs by trace Zn additions remain insufficiently understood, particularly in relation to their impact on nucleation, grain coarsening, and interfacial energy modulation.

This study addresses critical knowledge gaps by systematically investigating the role of Zn in the solidification and interfacial reactions of Sn–Cu–Zn solder alloys. Using model (Sn–Cu)–xZn/Cu systems, the effect of Zn on the development of both the as-solidified microstructure and the solder-substrate interfacial IMCs is explored. A mechanistic hypothesis is proposed wherein trace Zn alters the interaction between elements due to its affinity for Cu atoms. This may significantly alter the diffusion pathways, thermodynamics and kinetics of IMC formation. Especially, the formation of a thin Cu-Zn based intermetallic layer at the solder/Cu interface can significantly retard the formation of detrimental Cu-Sn based IMCs such as η and ε by creating a diffusion barrier and limiting Cu transport during prolonged thermal exposure. Advanced characterisation techniques are used to analyse the microstructures and reaction layers after reflow and aging to identify the nature and kinetics of IMC phases formed due to trace Zn addition. To complement and explain the experimental results, phase-field simulations are employed to clarify the phase formation and provide insight into the nucleation, growth, and evolution of interfacial IMCs. The simulations helped reveal how Zn influences solute gradients, phase stability and inhibit growth of specific IMCs, thereby clarifying the role played by Zn in the modified solder/substrate interactions. Together, the combined experimental and computational approach provides a comprehensive framework for designing high-reliability, Pb-free solder alloys for demanding thermal environments.

## 2. Materials and methods

### 2.1. Solder alloy preparation

Binary Sn–0.7Cu and ternary (Sn–0.7Cu)–xZn (x = 0.2, 0.5, 0.8, 1.0 wt%) solder alloys were prepared using commercially available high-purity metals (99.99 % Sn, Cu, and Zn). The required amounts of these elements were weighed using an analytical balance (precision ± 0.001 g) to ensure precise composition control. The weighed metals were placed in a high-temperature alumina crucible and melted in an electric resistance furnace set at 380 ± 3 °C. To ensure homogeneity, the molten alloy was mechanically stirred for 10 min using a zirconia-coated rod. The melt was maintained at the target temperature for an additional 60 min to allow complete dissolution of the alloying elements (especially Cu) and to stabilise the composition. The molten alloy was then cast into cylindrical ceramic mould with an inner diameter of 10 mm and a height of 20 mm. The cast samples were allowed to cool to room temperature under ambient conditions.

### 2.2. Solidification temperature measurement

Solidification temperatures were measured using a K-type calibrated thermocouple connected to a multichannel data logging system. Cooling curves were recorded during solidification to determine undercooling and nucleation temperature for phase transformations. Samples were cold mounted in resin for microstructural analysis. Phase transformations were further investigated using Differential Scanning Calorimetry (DSC). Approximately 25–30 mg of each alloy was selected, and DSC was performed between 25 °C and 250 °C under heating and cooling rates of 1 °C/min. This process was repeated three times to ensure repeatability and accuracy of the results. The Mettler Toledo DSC 822, calibrated for temperature and enthalpy, was used for this analysis, and no flux was employed during these experiments.

### 2.3. Preparation of solder samples

Cu-coated FR4 substrates were cut into 5 mm square plates, with a Cu thickness of 35 μm. Before reflow soldering, the substrates were cleaned sequentially with isopropyl alcohol (IPA), acetone, and deionised water to ensure a contaminant-free surface. For each solder alloy, 0.010 ± 0.003 g of material was cut from the solidified ingot, cleaned, and coated with a thin layer of Henkel LF318 flux. A solder layer, with a maximum thickness of 1 mm, was applied to the substrate, as shown in Fig. 1.

The soldering process was carried out in a benchtop reflow oven (MRO 160). The reflow profile consisted of a preheating stage at 140 °C

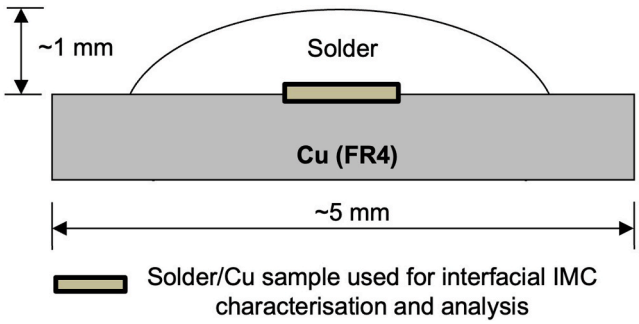


**Fig. 1.** Schematic cross-sectional geometry of the Sn–0.7Cu/Cu and (Sn-0.7Cu)–Zn/Cu samples.

for 150 s, followed by soldering at 260 °C for 60 s. After reflow, the solder joints were cooled to room temperature in air, and any residual flux was removed using acetone.

To simulate high-temperature service conditions, the samples were subjected to accelerated aging by heating in air at 150 °C for durations ranging from 1 to 1000 h. The aging experiments align with accelerated thermal aging standards, such as JEDEC JESD22-A103 (High Temperature Storage Life, HTSL). This thermal treatment allowed for the study of IMCs formation and growth kinetics under solid-state conditions, providing insight into long-term behaviour and reliability of the solder joints.

### 2.4. Identification and measurement of IMCs

Following aging experiments, samples were sectioned and polished to obtain smooth surfaces for microstructural investigation. Initially, specimens were sectioned using a precision saw and then polished sequentially with SiC papers followed by diamond suspensions (3 μm and 0.05 μm) to achieve a mirror finish.

Microstructural analysis was performed using a ZEISS Axio Lab. A1 optical microscope for low-magnification imaging and an FEI Quanta field emission gun scanning electron microscope (FEG SEM) for higher-resolution imaging. The FEG SEM was equipped with energy-dispersive X-ray spectroscopy (EDS) for element identification.

For detailed analysis of IMCs, scanning transmission electron microscopy (S/TEM) was conducted using a dual-beam focused ion beam (FIB-SEM) system (FEI Scios). Transmission electron microscopy (TEM) analysis was performed at 200 kV on a FEI Talos F200X microscope, equipped with a super-X EDS system consisting of four silicon drift detectors. High-angle annular dark-field (HAADF) and bright-field (BF) images were simultaneously acquired in STEM mode, while diffraction analysis was performed in conventional TEM mode to obtain crystallographic information. X-ray diffraction (XRD) measurements were carried out using an Anton Paar XRDynamic 500 diffractometers equipped with Co $K\alpha_{1/2}$ radiation. The sample height and flatness were carefully adjusted to ensure that the specimen surface was aligned with the goniometer's centre of rotation. Each scan was performed over approximately 4 h to achieve sufficient signal quality.

The average thickness of the IMC layers at the solder/substrate interface was measured using the Zeiss AxioVision image analysis software. The reported IMC thickness values are the average of measurements taken from at least three different samples, with a minimum of 50 individual measurements per sample. The error bars in the IMC thickness plots correspond to the 95 % confidence intervals.

For the top-view imaging of IMCs, the majority of the solder material was ground away, and the remaining solder was etched using 17 % nitric acid for approximately 30 min. This selective etching process allowed the visualisation of the IMC layer. The mean equivalent diameter of the η – $Cu_6Sn_5$ grains was calculated by counting the number of grains within the SEM images. The grain size was determined using the following equation:

$$\overline{d} = \sqrt{\frac{4S}{\pi N}} \tag{1}$$

where $d$ is the mean equivalent diameter, $S$ is the actual area of the SEM image and $N$ is the number of grains observed within the image area.

### 2.5. Computer simulation of IMC formation at the solder/substrate interface

The simulation of microstructural evolution was carried out using the phase-field approach [44–47]. In this model, the phase-field variables ($\varphi$) represent the fractions of different phases and grains within the system. The definitions are as follows: $\varphi_1$ corresponds to the phase fraction of the solid, $\varphi_N$ corresponds to the phase fraction of the liquid, and $\varphi_j$ ($j = 2,\cdots,N-1$) represents the phase fractions of individual grains of the η-phase. In this framework, the region where $\varphi_i = 1$ indicates the bulk of the $i-$ phase (or $i^{th}$ η grain), while the region where $0 < \varphi_i < 1$ corresponds to the interface or grain boundary adjacent to the $i$-phase (or $i-$ η grain). The interface is thus treated as a finite region where a mixture of different phases or grains coexists. To ensure physical consistency, the phase-field variables at any position in the system are subject to the constraint:

$$\sum_{i=1}^{N} \varphi_i(\vec{x}, t) = 1 \tag{2}$$

The total free energy of the system ($G$), accounting for spatial inhomogeneities in the Zn composition and phase-field variables ($\varphi_i$, where $i = 1, \ldots, N$), is formulated as a function of these variables and expressed through a volume ($V$) integral, as shown in equations (3)–(8) [45]:

$$\frac{\partial G}{\partial V} = f^P + f^T + \lambda_\varphi \sum_{i=1}^{N} (\varphi_i - 1) \tag{3}$$

$$f^P = \sum_{i=1}^{N} \varphi_i f_i(c_i) \tag{5}$$

$$f^T = \sum_{i=1}^{N} \sum_{j=i+1}^{N} \left(-\frac{\varepsilon^2_{ij}}{2} \nabla\varphi_i . \nabla\varphi_j + \omega_{ij}\varphi_i\varphi_j\right) \tag{6}$$

$$\partial G = \int_V [f^P + f^T + \lambda_\varphi \sum_{i=1}^{N} (\varphi_i - 1)]\partial V \tag{7}$$

$$G = \int_V [\sum_{i=1}^{N} \{\varphi_i f_i(c_i) + \sum_{j=i+1}^{N} (-\frac{\varepsilon^2_{ij}}{2} \nabla\varphi_i . \nabla\varphi_j + \omega_{ij}\varphi_i\varphi_j)\} + \lambda_\varphi \sum_{i=1}^{N} (\varphi_i - 1)]dV \tag{8}$$

where, $\lambda_\varphi$ is the Lagrange multiplier for the constraint, $f_i(c_i)$ is the chemical free energy density of $i-$ phase that depends on the phase composition ($c_i$), and $\varepsilon_{ij}$ and $\omega_{ij}$ are the boundary conditions (constant) along the IMC height, respectively. The parameters are associated with the interfacial energy between $\varphi_i = 1$ and $\varphi_j = 1$ phases (or grains).

The coexisting phases at a position in the interface region are assumed to have identical diffusion potential that is defined as the difference between the chemical potentials of the constituent species (Eq. (9) [48]):

$$\frac{\delta f_1}{\delta c_1} = \frac{\delta f_2}{\delta c_2} = \cdots = \frac{\delta f_N}{\delta c_N} = f'(x, \varphi_i) \tag{9}$$

The evolution of the composition field $c(\vec{x}, t)$ (equation (10) and the phase fields $\varphi_i(\vec{x}, t)$ with time is assumed to occur in such a way that total free energy of the system, $G$, decreases monotonically toward a minimum (equation (10) and (11), [48]):

$$c(\vec{x}, t) = \sum_{i=1}^{N} c_i\varphi_i \tag{10}$$

$$\frac{\delta c}{\delta t} = -\nabla . \vec{j} \tag{11}$$

With the flux $\vec{j}$ given by [45,48]:

$$\vec{j} = -M_c\left(c, \varphi_i, \varphi_j\right)\left(\frac{\delta F}{\delta c}\right) \tag{12}$$

and evolution of the phase-field Eq. (13) [45]:

$$\frac{\delta\varphi_i}{\delta t} = -\frac{2}{N_p}\sum_{i\neq j}^{N}\chi_i\chi_j L\left(c,\varphi_i,\varphi_j\right)\left(\frac{\delta F}{\delta\varphi_i}-\frac{\delta F}{\delta\varphi_j}\right) \quad (13)$$

Here, $M_c$ represents the atomic mobility, and $L\left(c,\varphi_i,\varphi_j\right)$ is the relaxation coefficient associated with $\varphi_i$ and $\varphi_j$, which can depend on c, $\varphi_i$ and $\varphi_j$, and $t$ denotes time. The parameters $\chi_i$ and $\chi_j$ are set to 1 when the respective phase is present and to 0 otherwise. $N_p$ represents the number of coexistent phases.

The stochastic nature of grain nucleation was modelled using a Poisson distribution ($P_m$) to represent the probability of "minus zero" events, as described in equation (14) and (15). This approach captures the inherent randomness of nucleation events, allowing for a more realistic simulation of the microstructure evolution.

$$P_n = 1 - e^{-J\nu\Delta t} \quad (14)$$

$$J = J_o e^{-\frac{4\pi\sigma^3(\cos\theta^3-3\cos\theta+2)}{3kT(\Delta G_V)^2}} \quad (15)$$

where, $\Delta t$ is the time interval, $\nu$ is the nucleation volume, $J_o$ is the nucleation frequency factor, $\sigma$ is the energy of the solid/liquid interphase, $k$ is Boltzmann constant, $\theta$ is the nucleation angle, $T$ is the temperature and $\Delta G_V$ is the driving force between crystal/liquid. $J_o$, $\sigma$ and $\theta$ were set at $1.0 \times 10^{29}$ m/s, 0.346 J/m$^2$ and 296 K, respectively. $\Delta G_V$ for each phase is calculated using the equations and parameters from the literature (Table 1). The crystalline phases nucleated were identified as β −Sn, η-$Cu_6Sn_5$, and γ-$Cu_5Zn_8$, and their nucleation probability was determined by the $\Delta G_V$.

The simulation domain consisted of 200 mesh elements along the X-axis and 90 meshes along the Y-axis, with each mesh having a size of $5 \times 10^{-8}$ m. The Cu solid region was defined from meshes 0 to 32 along the Y-axis, while the liquid region occupied meshes 32 to 90, forming a solid/liquid interface layer between meshes 30 and 32. Neumann boundary conditions were applied to the top and bottom of the domain, while periodic boundary conditions were implemented along the sides. The incubation time, representing the period before nucleation and diffusion processes began, was set to 8 s [53]. All molar volumes were assumed to have a uniform value of 16.29 cm$^3$/mol.

The equilibrium phase compositions ($c_{a-bc}$) at the soldering temperature (523 K) during the incubation step are presented in Table 2. In this notation, a represents the phase, while bc denotes the interphase, where b is the predominant phase and c is the minority phase. These compositions were determined using the CALPHAD method [52,54]. The liquid phase is represented as L (solder), while the solid phases are α (Cu), η- and γ-IMC.

**Table 1**
Parameters used for simulating IMC formation and growth during soldering at 530 K from literature [46,49–52].

| Phase | Phase diffusion (m$^2$/s) | Atomic mobility (m$^2$/s) | Interphase energy (J/m$^2$) |
|---|---|---|---|
| Solid (β-Sn) | $2.0 \times 10^{-18}$ [47,53] | – | – |
| Liquid (Solder) | $2.0 \times 10^{-12}$ [47,53] | – | – |
| η-$Cu_6Sn_5$ | $4.0 \times 10^{-17}$ [47] | – | – |
| η-$Cu_6Sn_5$ in liquid | $2.0 \times 10^{-13}$ [47] | $2.0 \times 10^{-6}$ [47] | 0.100 [47,51] |
| η-$Cu_6Sn_5$ in solid | $4.0 \times 10^{-15}$ [47] | $1.4 \times 10^{-7}$ [47] | 0.300 [47,51] |
| η-$Cu_6Sn_5$ grain boundary | $4.0 \times 10^{-14}$ [47] | $1.4 \times 10^{-7}$ [47] | 0.300 [51,53] |
| γ-$Cu_5Zn_8$ | $2.6 \times 10^{-18}$ [47,53] | – | – |
| γ-$Cu_5Zn_8$ in liquid | $1.3 \times 10^{-14}$ [47] | $1.3 \times 10^{-7}$ [47] | 0.121 [50,52,53] |
| γ-$Cu_5Zn_8$ in solid | $2.6 \times 10^{-16}$ [47] | $9.1 \times 10^{-9}$ [47] | 0.076 [50,52,53] |
| γ-$Cu_5Zn_8$ grain boundary | $2.6 \times 10^{-15}$ [47] | $9.1 \times 10^{-9}$ [47] | 0.150 [50] |
| Cu (solid)/Solder (liquid) | – | – | 0.346 [47, 52 50] |

**Table 2**
The equilibrium phase compositions for the initial step of the soldering simulations.

| | |
|---|---|
| $c_{L-L\eta}$ | 0.977 |
| $c_{\eta-L\eta}$ | 0.436 |
| $c_{L-\alpha L}$ | 0.977 |
| $c_{\alpha-\alpha L}$ | 0.001 |
| $c_{\gamma-\gamma L}$ | 0.710 |
| $c_{L-\gamma L}$ | 0.977 |
| $c_{\gamma-\gamma\alpha}$ | 0.001 |
| $c_{\alpha-\gamma\alpha}$ | 0.999 |

## 3. Results

### 3.1. Microstructural formation in Sn–Cu–xZn solder alloys

The solidification behaviour of the Sn–0.7Cu alloy system is dominated by the eutectic reaction L→β −Sn + η −$Cu_6Sn_5$ at 227 °C. The as-solidified microstructure of Sn–0.7Cu (Fig. 2**(a2-e2)**) reveals primary β −Sn grains surrounded by a eutectic mixture of β −Sn + η −$Cu_6Sn_5$. The eutectic growth in the Sn–Cu system exhibits two distinct morphologies: a fine eutectic structure, typically observed in the interdendritic regions, characterised by closely spaced η and Sn phases; and a course, faceted η-phase morphology, which often forms at grain boundaries or in areas of slower solidification.

The addition of Zn significantly modifies the microstructural evolution, as shown in Fig. 2**(b2–e2)**. Even minor Zn additions alter the eutectic regions, with Zn incorporating into the η −phase and inducing a secondary solidification reaction. *Insitu* synchrotron radiography observations [16] of the Sn–0.7Cu–0.15Zn alloy reveal the formation of a CuZn(Sn) phase during solidification, following the reaction L + $Cu_6(Sn,Zn)_5$→β − Sn + CuZn. The formation of CuZn phases typically requires a Zn content of ≥ 0.5 wt% in the solder alloy.

The microstructure evolves further as the Zn content increases. Alloys with Zn additions in the range of 0.2–0.5 wt% exhibit a notable refinement of the eutectic structure and the appearance of CuZn-based IMCs. Although quantitative metrics are not applicable due to the fibrous eutectic morphology, refinement is established through microstructural evidence showing reduced fiber continuity and increased phase dispersion. At 1 wt% Zn (Fig. 2**(e2)**), the microstructure is characterised by uniformly distributed eutectic and the formation of γ-$Cu_5Zn_8$ particles within the β −Sn matrix. These particles form via a quasiperitectic reaction: (L + η→CuZn + β −Sn; L + CuZn→β −Sn + γ − $Cu_5Zn_8$; L + γ − $Cu_5Zn_8$→β −Sn + $CuZn_4$) and ternary eutectic reaction (L→β −Sn +Zn +$CuZn_4$) [16,55,56].

Detailed microstructural analysis of the 1 wt% Zn alloy reveals primary γ-IMC particles at the centres of β −Sn dendrites (Fig. 2**(e2)**). Further observation indicates multiple γ particles within individual β −Sn grains, suggesting these IMCs may not serve as effective nucleation site for β −Sn, consistent with earlier findings for η −phase in similar systems [57]. These results emphasise the role of Zn in refining the eutectic morphology and influencing IMC distribution, thereby enhancing the alloy's microstructural uniformity and potential soldering performance.

### 3.2. Thermal analysis results

The thermal behaviour of (Sn–0.7Cu)–xZn solder alloys was investigated using cooling curves (Fig. 2**(a1-e1)**) and DSC (Fig. 3). These methods provided insight into the solidification and melting transformations of β −Sn and eutectic phases across varying Zn concentrations.

**Heating and cooling transformations:** The DSC traces for all solder compositions during heating and cooling cycles are presented in Figs. 3 (a) and (b), highlighting endothermic peaks on heating and exothermic

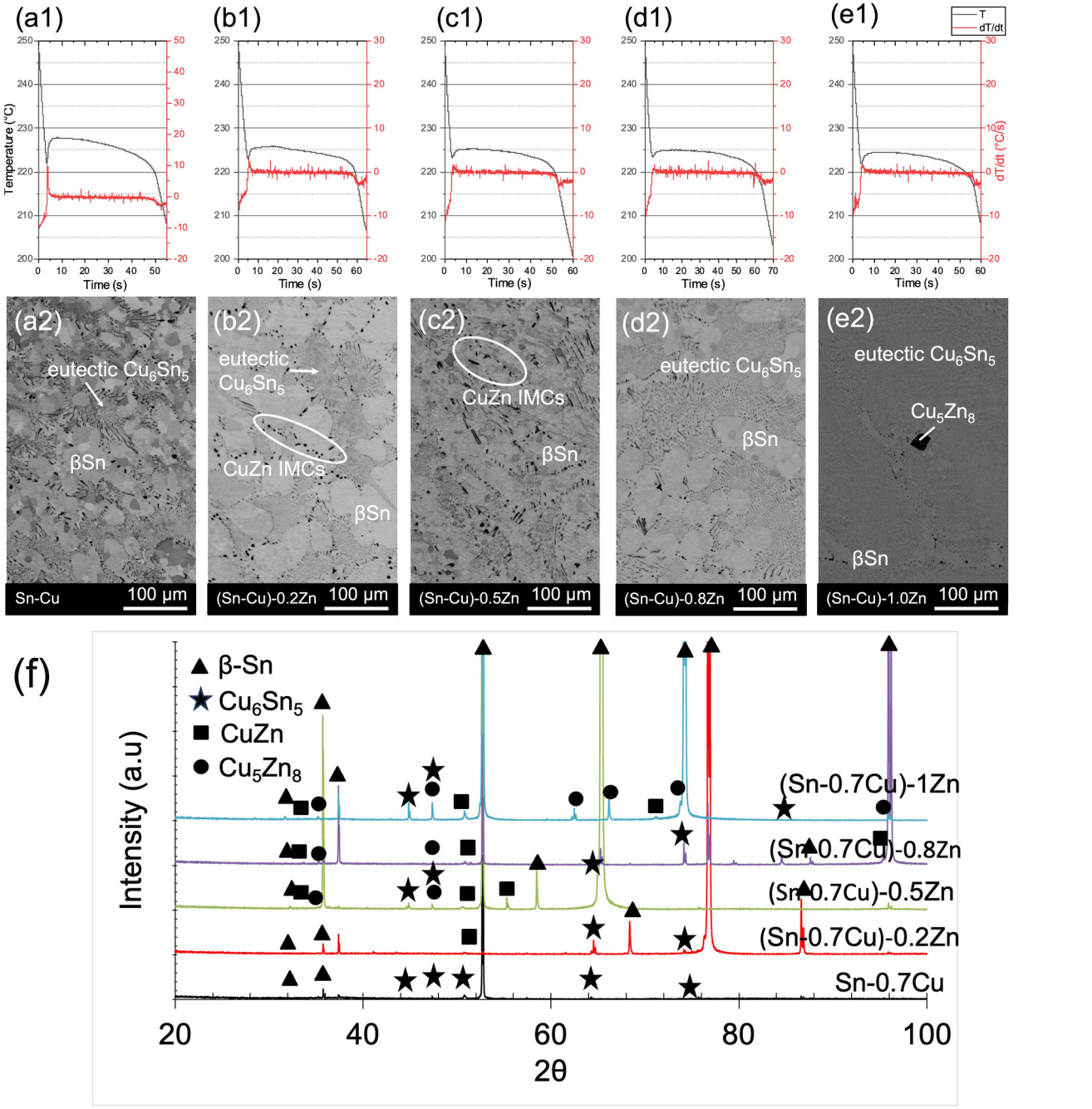


**Fig. 2.** (a1-e1) Cooling curves recorded during the solidification of Sn–0.7Cu and (Sn–0.7Cu)–xZn alloys (x = 0.2, 0.5, 0.8, and 1 wt%) highlighting nucleation and phase transformation events. Corresponding micrographs illustrate the microstructure of (a2) Sn–0.7Cu, (b2) (Sn–0.7Cu)–0.2Zn, (c2) (Sn–0.7Cu)–0.5Zn, (d2) (Sn–0.7Cu)–0.8Zn, and (e2) (Sn–0.7Cu)–1.0Zn alloys, showcasing the evolution of primary β −Sn, eutectic regions, and Zn-modified IMCs with increasing Zn content. EDS analysis confirmed the presence of these phases. (f) XRD analysis of all solder samples, confirmed presence of the CuZn and $Cu_5Zn_8$ IMCs.

freezing peaks on cooling. These peaks correspond to the melting and solidification of β −Sn and the eutectic phase, respectively. The onset temperatures for melting ($T_L$) and solidification ($T_S$) were recorded, revealing the influence of Zn addition on these transformations (Fig. 4 (b)). The onset of melting ($T_L$) decreased slightly with initial Zn addition but remained relatively stable for Zn levels between 0.2 and 0.8 wt%. However, the onset of solidification ($T_S$) increased significantly compared to the Zn-free Sn–Cu alloy, indicating improved nucleation behaviour. A distinctive low-temperature peak (~198 ± 1 °C) observed in the 1 wt% Zn alloy thermograms (marked in Fig. 3) corresponds to the solidification of the $Cu_xZn_{1-x}$. The small magnitude of this peak suggests the limited presence of this phase in the alloy, consistent with expectations.

**Undercooling and nucleation behaviour**: Cooling curve derivatives (Fig. 2**(a1-e1)**) revealed major nucleation events during solidification. Zn addition up to 0.8 wt% markedly reduced the undercooling required for β −Sn nucleation. Fig. 4(a) shows the nucleation temperature increasing with Zn content, with a notable decrease in undercooling for compositions between 0.2 and 0.8 wt% Zn. However, the addition of 1 wt% Zn slightly increased undercooling for β −Sn nucleation, possibly due to the formation of primary γ-phase that reduce the availability of Zn solute for nucleation. The nucleation undercooling ($\Delta T = T_L - T_S$) calculated from DSC traces confirms this trend. Zn additions reduced ΔT significantly by 35–40 °C, indicating a pronounced

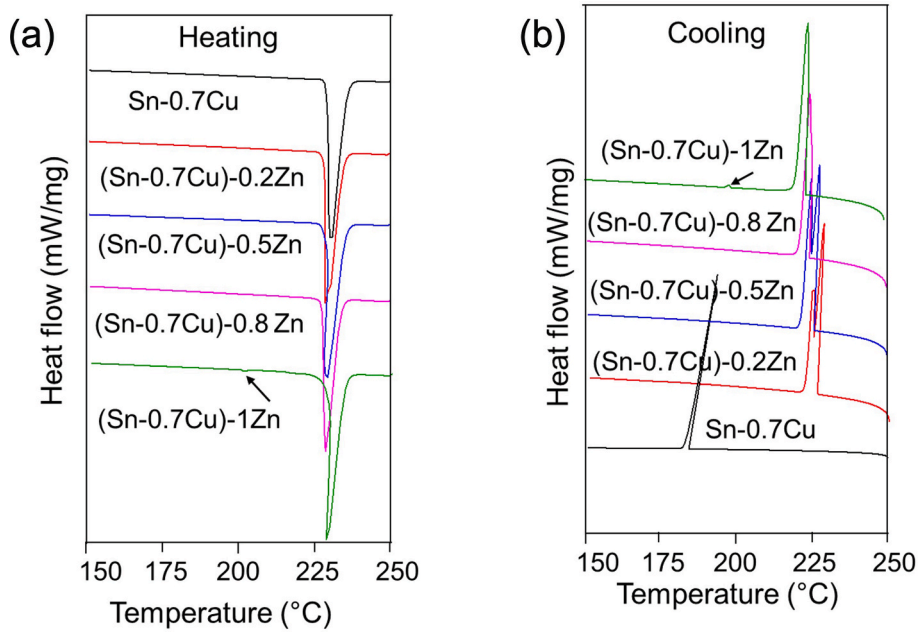


**Fig. 3.** DSC traces for (Sn–0.7Cu)–xZn alloys recorded at a scan rate of 1 K/min: (a) heating curves showing phase transformation temperatures and (b) cooling curves highlighting solidification events.

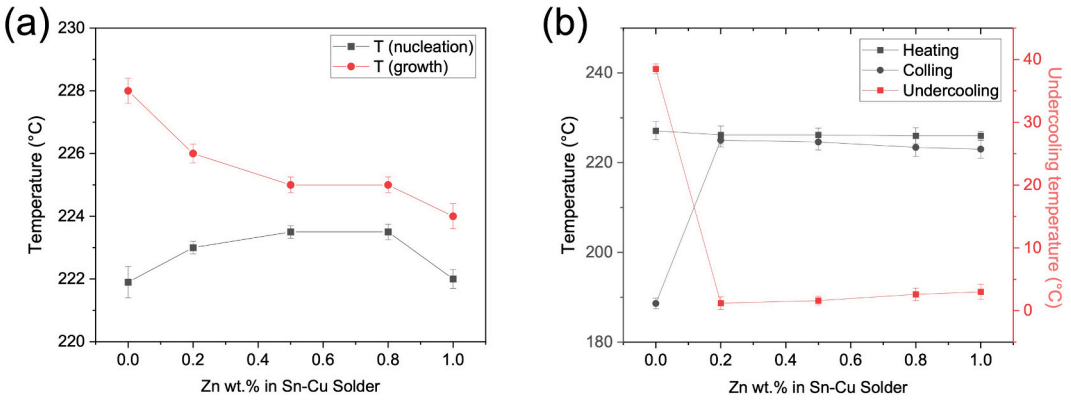


**Fig. 4.** Summary of thermal analysis results: (a) nucleation temperatures extracted from cooling curves in Fig. 2, and (b) melting, solidification, and undercooling temperatures ($\Delta T = T_L - T_S$) derived from the DSC traces in Fig. 3.

effect on β −Sn nucleation. In the Zn-free Sn–Cu alloy, a large temperature difference between solidification and melting was observed, reflecting higher undercooling requirements. Zn additions mitigate this, enhancing nucleation by lowering the energy barrier for β −Sn formation.

**Role of Zn in promoting nucleation**: Zn promotes nucleation through two potential mechanisms. First, ZnO particles introduced by Zn additions may act as potent nucleation sites for β −Sn [58]. The orientation relationship between β −Sn and ZnO, reported in previous studies, demonstrates excellent lattice matching: $[100]\beta - Sn \parallel [1\bar{2}13]$ZnO with a misfit of 5.29 % and $(011)\beta - Sn \parallel (10\bar{1}0)$ ZnO with a mismatch of 1.24 % [16]. These findings support the hypothesis that ZnO enhances nucleation. Second, Zn acts as a growth-restricting solute, creating constitutional undercooling that facilitates the nucleation of β −Sn [34]. This dual role of Zn in modifying the solidification pathway highlights its critical influence on the microstructural evolution of (Sn–0.7Cu)–xZn solder alloys.

### 3.3. Liquid–state reaction between solder and substrate

Fig. 5 presents detailed micrographs of the as-reflowed solder joints, revealing the microstructural evolution during the reflow process. In the Sn-0.7Cu solder matrix, the β −Sn dendrites are surrounded by a eutectic mixture of $Cu_6Sn_5$, similar to the as-solidified microstructure of the solder alloy. A relatively thin nodular IMC layer forms at the solder/substrate interface during the reflow process. EDS analysis (Fig. 5(a)) indicates that a layer of η-phase, approximately 3 μm thick, forms rapidly at the interface in the Sn-0.7Cu/Cu system. Furthermore, ε-IMCs may also form at the interface of the solder and Cu substrate.

The formation of the IMC layer is predominantly heterogenous and random, as evidenced by the irregular growth of the η-IMC at different sites. The rapid formation of the ε-IMC (as shown later in Fig. 7, the layer is ~ 90 nm thick) in the partially molten solder suggests that the rate of nucleation and growth is extremely high in the liquid state. The presence of the ε-IMC is particularly significant, as it is known to influence the long-term reliability of solder joints by affecting the mechanical properties and thermal stability.

When Zn is introduced into the Sn-0.7Cu solder, the interfacial IMC

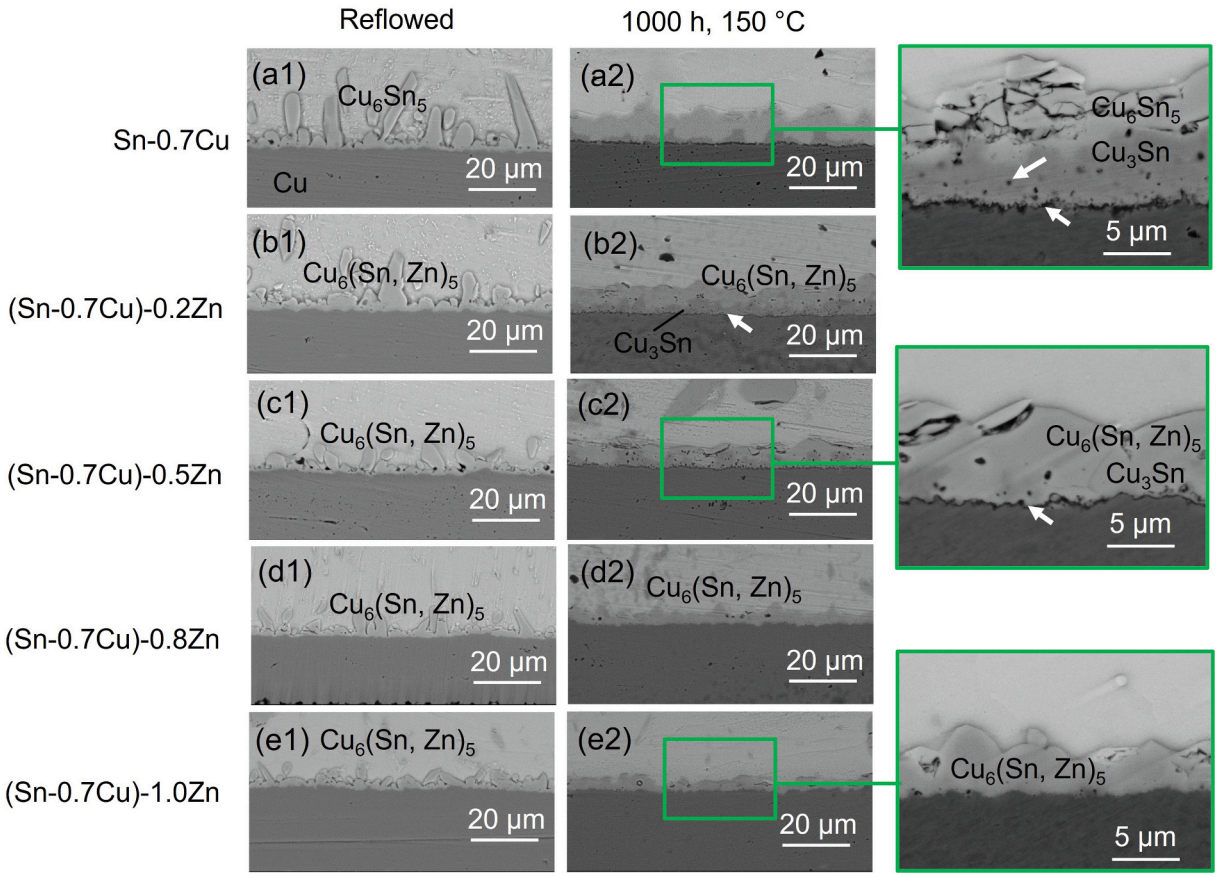


**Fig. 5.** Cross-sectional microstructure of solder/substrate interfaces for as (a1) –(e1) reflowed and (a2)-(e2) thermally aged (150 °C for 1000 h) samples. Arrows in high magnification image of (a2)–(c2) indicate Kirkendall voids and cracks observed at the interfaces.

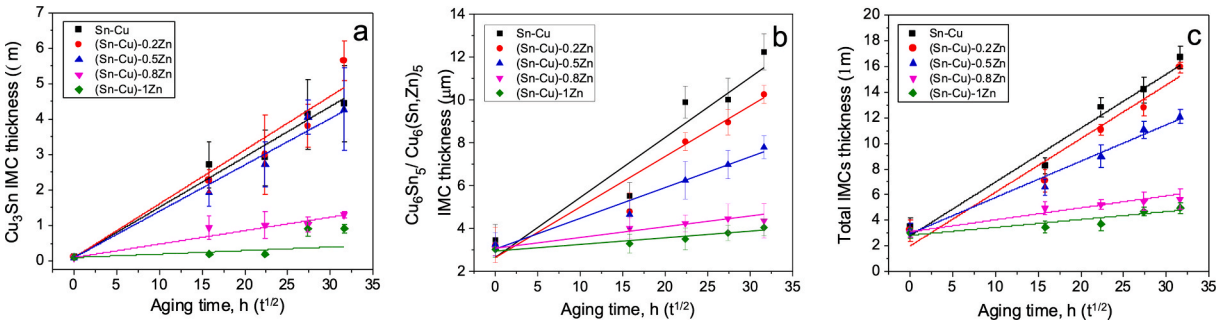


**Fig. 6.** Evolution of IMC layer thickness with aging time at 150 °C: (a) ε-$Cu_3Sn$, (b) η-$Cu_6Sn_5$/$Cu_6$ $(Sn,Zn)_5$, and (c) total IMC thickness. Data points affected by spalling were excluded from the analysis.

layer becomes finer, and the growth of long IMC particles at the interface is suppressed. This effect is clearly shown in Fig. 5**(c) to (e)**, where the microstructure of the reflowed solder joints with varying Zn content exhibits a reduction in the size and elongation of the interfacial IMC particles. EDS analysis of these samples confirms the incorporation of Zn into the interfacial η-IMC (called the $Cu_6(Sn, Zn)_5$ IMC henceforth). As shown in Table 3, the Zn concentration in the interfacial IMC increases with the Zn content in the original solder matrix. Specifically, the Zn concentration ranges from 0.4 to 2.64 at. %, as the Zn content in the solder increases from 0.2 wt% to 1 wt%. This finding supports the idea that Zn plays a crucial role in modifying the interfacial IMC structure by enhancing the dissolution of Zn in the η- phase.

### 3.4. Solid–state reaction between solder and substrate

Following the initial formation of η- and ε-phases during the liquid-state reaction between Sn and Cu, thermal aging promotes further Sn and Cu interdiffusion, which leads to the growth of these phases at the solder/substrate interface. The growth of the η phase is facilitated by the diffusion of Cu through the existing ε- and η-phases, reacting with Sn at the η/Sn interface, while Sn diffuses through the η-phase and reacts with Cu at the ε/η interface. Similarly, the growth of the ε-phase occurs as Cu and Sn diffuse through the η and ε-IMC, reacting at the ε/η interface, with Sn also diffusing through ε to react at the Cu/ε interface. At 150 °C, Cu interstitial diffusion is expected to dominate, while at higher temperatures (≥ 180 °C), Sn vacancy diffusion is favoured [23]. During the solid-state aging process, the grain boundaries act as channels within the IMC layer serve as the primary diffusion pathways for IMC growth,

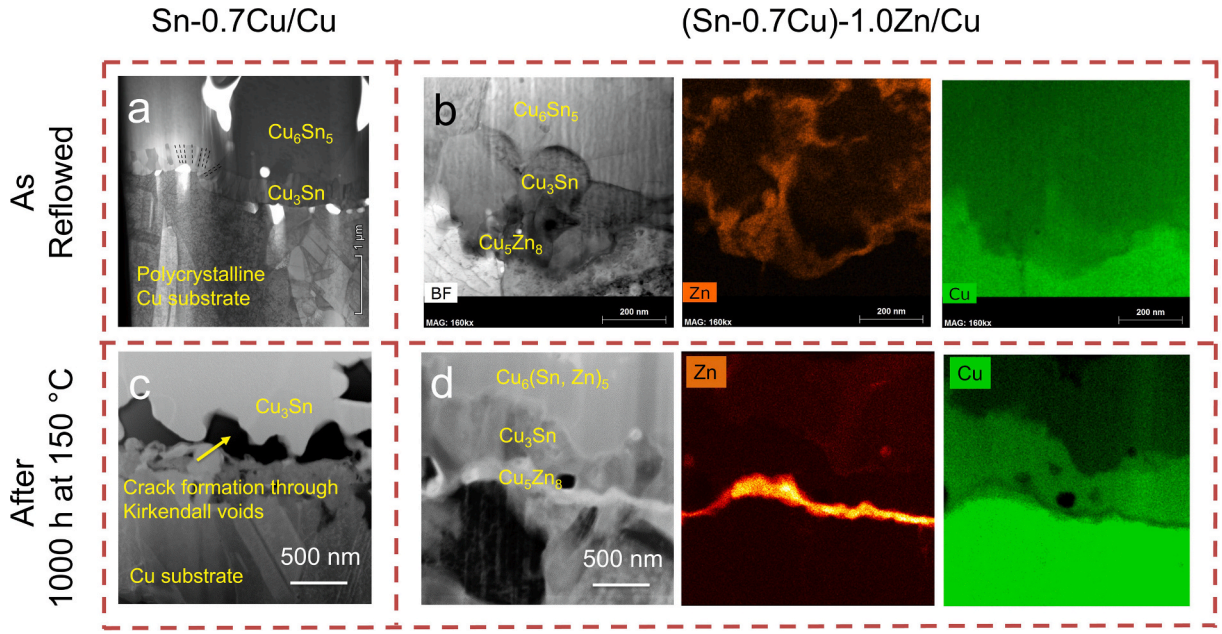


**Fig. 7.** TEM analysis of Sn-0.7Cu/Cu and (Sn-0.7Cu)-1.0Zn/Cu interfaces after reflow and aging at 150 °C: (a, b) Cross-sectional views of the as-reflowed samples show a ~ 100 nm thick γ-$Cu_5Zn_8$ IMC layer in the Zn-containing system; (c, d) Cross-sectional views after 1000 h aging reveal significant ε-$Cu_3Sn$ IMC growth and crack formation via Kirkendall voids in the Sn-0.7Cu system. In contrast, the Zn-containing solder exhibits a thinner ε −$Cu_3Sn$ IMC, reduced Kirkendall voids, and increased γ-$Cu_5Zn_8$ IMC thickness.

**Table 3**
Chemical composition of interfacial η-$Cu_6Sn_5$ IMC in as-reflowed samples and after 1000 h of thermal aging at 150 °C.

| Solder/Cu | As-reflow (0 h) (at. %) | | | 150 °C, 1000 h (at. %) | | |
|---|---|---|---|---|---|---|
| | Sn | Cu | Zn | Sn | Cu | Zn |
| Sn-0.7Cu/ Cu | 46.26 ± 0.9 | 53.74 ± 1.4 | – | 35.90 ± 0.6 | 64.10 ± 0.7 | – |
| (Sn-0.7Cu)-0.2Zn/Cu | 47.39 ± 0.9 | 53.21 ± 1.1 | 0.4 ± 0.1 | 38.90 ± 0.8 | 60.21 ± 1.1 | 0.89 ± 0.5 |
| (Sn-0.7Cu)-0.5Zn/Cu | 43.44 ± 1.0 | 55.41 ± 1.7 | 01.15 ± 0.4 | 38.72 ± 1.2 | 59.82 ± 1.9 | 01.45 ± 0.3 |
| (Sn-0.7Cu)-0.8Zn/Cu | 44.02 ± 0.8 | 54.07 ± 1.3 | 01.91 ± 0.2 | 47.15 ± 1.9 | 50.20 ± 2.3 | 02.66 ± 0.8 |
| (Sn-0.7Cu)-1.0Zn/Cu | 42.29 ± 0.8 | 55.08 ± 2.4 | 02.64 ± 0.7 | 40.35 ± 2.1 | 55.30 ± 1.7 | 04.35 ± 1.1 |

suggesting that the grain morphology and the area percentage of grain boundaries are critical factors in determining the behaviour of IMC growth.

Fig. 5 summarises typical aged microstructures after thermal aging at 150 °C for 1000 h. As shown, the microstructure of the unmodified Sn-0.7Cu solder alloy is compared with that of the modified alloys. Microcracks along the ε/Cu interface were observed in the Sn-0.7Cu, (Sn-0.7Cu)-0.2Zn, and (Sn-0.7Cu)-0.5Zn solders after 1000 h of aging. The interfacial region in Fig. 5 reveals Kirkendall voids and cracks marked by arrows in Figs. 5(a) to 5(c). In particular, Fig. 5(a) shows a complete debonding with excessive growth of both η and ε-IMCs. High-magnification TEM images in Fig. 7(c) confirm this observation, where the crack location is highlighted. In contrast, Figs. 5(d) and 5(e) show significantly fewer interfacial voids and no evidence of extended coalescence of these voids (as further confirmed in high-magnification interfacial images in Fig. 7(d), explored systematically below in Section 3.5). These differences suggest that Zn addition reduces the growth of interfacial voids, which is critical for improving solder joint reliability.

The Kirkendall effect, a phenomenon resulting from the unequal diffusivities of Sn and Cu in the diffusion couple, leads to a supersaturation of lattice vacancies, particularly during the η to ε-IMCs transformation. The presence of Kirkendall voids is an important indicator of this effect, which can negatively impact the mechanical integrity of the solder joint. The addition of Zn effectively suppresses the formation and growth of these voids, reducing the detrimental effects of the Kirkendall effect.

Quantitative analysis of the IMC thickness data, shown in Fig. 6 and summarised in Table 4, reveals the impact of Zn addition on the IMC growth behaviour during solid-state aging. In the Sn-0.7Cu/Cu system, the total thickness of the η and ε-IMC layers increases significantly with aging, growing from approximately 3 μm to 8 μm after 250 h. The aspect ratio (height/diameter) of these IMCs increases with higher Zn content in the solder after reflow. However, during aging, this trend reverses as Zn suppresses both the growth (thickness) and coarsening of the IMCs. Notably, the addition of 0.8 wt% Zn leads to a reduction in IMC thickness, with an even more pronounced effect observed at 1.0 wt% Zn. This indicates that Zn inhibits the growth of interfacial IMCs, thereby mitigating potential embrittlement caused by the thickening of the IMC layers during aging.

The growth of the ε-IMC layer is significantly suppressed in the presence of Zn, even after 1000 h of aging. As seen in Figs. 5(d) and 5(e), the growth of the combined ε + η IMC layer is most effectively restricted by the addition of 1.0 wt% Zn. This observation highlights that 1 wt% Zn is the most effective composition for reducing the growth of the interfacial IMC layers during thermal aging. The growth kinetics of the IMCs follow diffusion-controlled Fick's law, expressed as:

$$d = (Dt)^{1/2} \tag{16}$$

where $d$ is the average thickness of the IMCs, $D$ is the diffusion-related growth rate constant, and $t$ is the aging time. The values of $D$ for the ε, η, and total IMCs are summarised in Table 5. It is evident that the diffusion coefficient $D$ decreases with increasing Zn concentration in the solder, further supporting the conclusion that Zn inhibits the growth of interfacial IMCs by restricting the diffusion of the constituent elements. This suppression of IMC growth is particularly advantageous for enhancing the long-term reliability of Sn-0.7Cu-based solder joints in electronic applications.

**Table 4**
Statistical analysis results for the total thickness, radius, and particle density of IMCs in (Sn–0.7Cu)–xZn/Cu samples, measured using the image analysis method.

| Solder/Cu | TotalIMCs thickness, h (μm)* | | | IMC diameter, d (μm) | | | Aspect ratio | Number of particles ($mm^2$) |
|---|---|---|---|---|---|---|---|---|
| | Mean | SD | CV | Mean | SD | CV | h/d | |
| After reflowing | | | | | | | | |
| (Sn-0.7Cu)/Cu | 3.46 | 0.73 | 0.21 | 4.42 | 1.40 | 0.63 | 0.8 | 28,754 |
| (Sn-0.7Cu)-0.2Zn/Cu | 3.23 | 0.83 | 0.26 | 4.28 | 1.50 | 0.70 | 0.8 | 31,601 |
| (Sn-0.7Cu)-0.5Zn/Cu | 3.26 | 0.55 | 0.17 | 3.38 | 1.14 | 0.68 | 1.0 | 37,295 |
| (Sn-0.7Cu)-0.8Zn/Cu | 3.04 | 0.30 | 0.10 | 2.34 | 0.87 | 0.74 | 1.3 | 96,797 |
| (Sn-0.7Cu)-1.0Zn/Cu | 3.02 | 0.37 | 0.12 | 1.98 | 0.30 | 0.31 | 1.5 | 99,359 |
| After aging at 150 °C for 1000 h | | | | | | | | |
| (Sn-0.7Cu)/Cu | 16.67 | 0.84 | 0.05 | 9.54 | 1.35 | 0.28 | 1.7 | 20,071 |
| (Sn-0.7Cu)-0.2Zn/Cu | 15.91 | 0.72 | 0.05 | 7.52 | 1.25 | 0.33 | 2.1 | 25,338 |
| (Sn-0.7Cu)-0.5Zn/Cu | 12.06 | 0.54 | 0.04 | 6.24 | 1.05 | 0.34 | 1.9 | 34,021 |
| (Sn-0.7Cu)-0.8Zn/Cu | 5.66 | 0.80 | 0.14 | 5.17 | 0.86 | 0.33 | 1.1 | 62,491 |
| (Sn-0.7Cu)-1.0Zn/Cu | 4.96 | 0.40 | 0.08 | 4.58 | 0.56 | 0.24 | 1.1 | 82,562 |

*Total IMC thickness measured by using η-$Cu_6Sn_5$ + ε-$Cu_3Sn$ or $Cu_6(Sn, Zn)_5$ + ε-$Cu_3Sn$ IMCs; SD and CV stand for standard deviation and coefficient of variation, respectively.

**Table 5**
Growth rate constants of IMCs ($cm^2/s$) as a function of Zn concentration.

| Solder/Cu | ε-$Cu_3Sn$ | η-$Cu_6Sn_5$ or $Cu_6(Sn, Zn)_5$ | Total |
|---|---|---|---|
| (Sn-0.7Cu)/Cu | $1.55 \times 10^{-17}$ | $6.05 \times 10^{-17}$ | $1.35 \times 10^{-16}$ |
| (Sn-0.7Cu)-0.2Zn/Cu | $1.77 \times 10^{-17}$ | $4.30 \times 10^{-17}$ | $1.34 \times 10^{-16}$ |
| (Sn-0.7Cu)-0.5Zn/Cu | $1.32 \times 10^{-17}$ | $1.59 \times 10^{-17}$ | $6.15 \times 10^{-17}$ |
| (Sn-0.7Cu)-0.8Zn/Cu | $1.11 \times 10^{-18}$ | $1.95 \times 10^{-18}$ | $6.73 \times 10^{-18}$ |
| (Sn-0.7Cu)-1.0Zn/Cu | $7.49 \times 10^{-20}$ | $7.39 \times 10^{-19}$ | $6.91 \times 10^{-18}$ |

### 3.5. Detailed characterisation of interfacial IMCs with simulation results

The interfacial structure of the solder joints was investigated in-depth using STEM and phase-field simulations to study the evolution of IMCs during reflow and aging. SEM analysis revealed a relatively thick η-IMC layer at the solder-substrate interface after reflow, which is easily detectable, while the ε and CuZn IMCs, which form between the Cu substrate and the η-IMC, were often too thin to be observed with SEM alone. To overcome this limitation, detailed STEM analyses were performed on selected samples, which provided higher-resolution insights into the microstructure and the evolution of these phases over time.

STEM-EDS mapping (Fig. 7) identified two distinct IMCs in the Sn-0.7Cu/Cu system: η and ε phase. In contrast, the (Sn-0.7Cu)-xZn/Cu system exhibited a third IMC, γ- phase), which was found to form as a thin, undulant, scallop-shaped layer (<100 nm thick) directly at the Cu interface (Fig. 7(b) and Fig. 8(a)). The presence of this CuZn IMC layer significantly inhibits the growth of ε and η-IMCs, as it restricts Cu diffusion, which is essential for the formation of these phases. Furthermore, Zn diffusion was observed to form CuZn at the interface, further blocking the flow of Sn from the solder to the Cu substrate, thus slowing the growth of ε- and η-phases (Fig. 7(b) EDS mapping). This phenomenon is corroborated by the STEM images presented in Fig. 8, where Zn and Sn elemental maps show the clear formation of CuZn at the interface (Fig. 8(c)).

Diffraction pattern analysis of the interfacial grains (Fig. 8(c)) revealed that the observed IMC phases (η, ε, and γ); match the predicted crystallographic structures, with diffraction patterns indexed to zone axes of $< 01\bar{1}0 >$, $< 0\bar{1}1 >$, and $< 511 >$, respectively. Notably, the grains of the η- and ε-phases exhibit an orientation relationship of $\{\bar{2}00\}//\{\bar{1}011\}$, though no distinct correlation was observed between

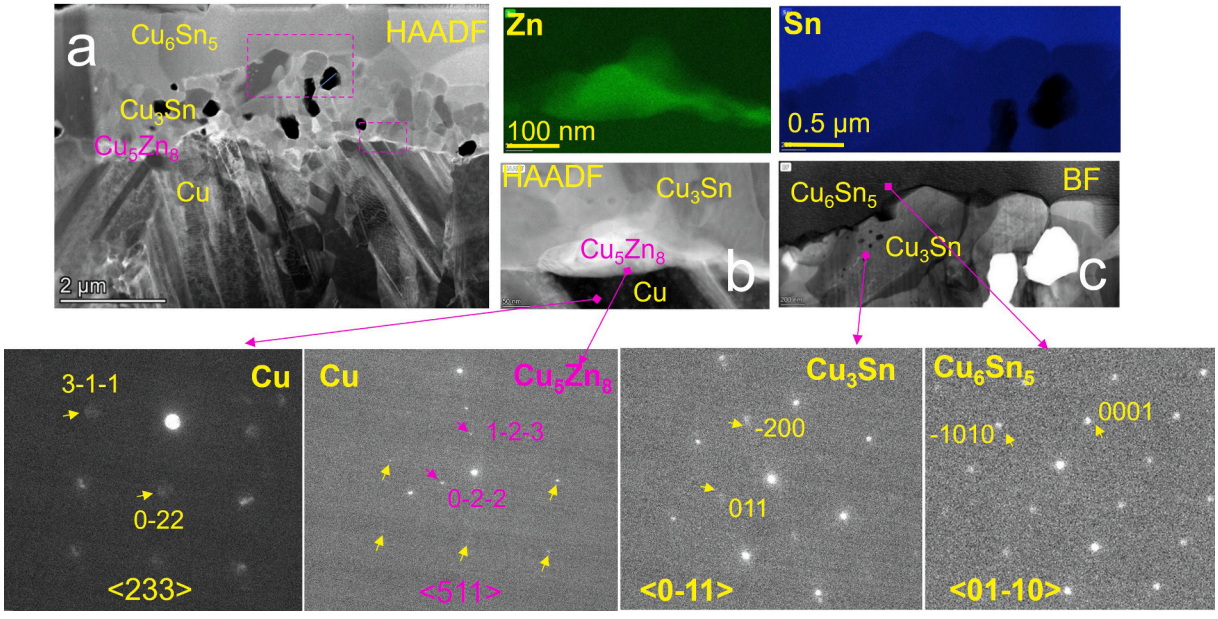


**Fig. 8.** TEM images of the (Sn-0.7Cu)-1.0Zn/Cu interface, showing detailed microstructures with corresponding diffraction patterns for each individual IMC layer.

the γ and Cu substrate grains, suggesting a more complex interaction at the interface.

To further analyse the morphology of the η-phase, selective etching was applied to expose the IMC layers following reflow (Fig. 9). The scalloped morphology of the η-phase is clearly visible, with individual grains separated by deep channels. This morphology typically forms during grain coarsening, not during nucleation [46]. Our phase-field simulation results support this observation, as they show a transition from prism-type η grains to the scalloped shape as reflow time increases. The simulations capture the grain boundary movement and surface diffusion processes that lead to this coarsening-driven transformation. The channels between the grains are attributed to grain boundary grooving, a thermodynamically driven phenomenon that occurs in solid–liquid couples. The varying angles of the grooves indicate the different crystallographic conditions of the grains.

The addition of Zn significantly influenced the formation of the η phase. As shown in Fig. 10, the number density of η grains increased with Zn content, and the coarsening of these grains was suppressed compared to the reference Sn-0.7Cu system during reflow and after thermal aging at 150 °C for 1000 h. This suggests that Zn plays a key role in limiting grain coarsening, which is crucial for the stability and reliability of the solder joint. In the phase-field simulations, Zn addition led to a larger number of smaller η grains, in contrast to the conventional Sn-0.7Cu solder, where larger grains are observed. These results are consistent with the experimental data and suggest that Zn limits the diffusion of Cu into the Sn matrix, thereby suppressing the growth of η and ε-IMCs.

In summary, both the experimental and simulation results demonstrate that the presence of γ-IMC at the interface significantly influences the nucleation and growth of ε and η-IMCs. The addition of Zn to the solder alloy not only enhances the number density of η grains but also prevents excessive grain coarsening, leading to more stable interfacial structures.

## 4. Discussion

This study combined experimental observations with phase-field simulations to reveal the influence of Zn on interfacial IMC nucleation, growth, and suppression in Sn-0.7Cu solder systems. The phase-field model accurately predicted phase evolution at the Cu interface, aligning well with experimental observation and validating the simulation's reliability in capturing the effects of Zn on interfacial IMC evolution.

During reflow, Cu rapidly dissolves into the liquid solder until the solder becomes supersaturated at the Cu/liquid solder interface. This supersaturation, combined with the thermodynamic driving force, leads to the formation of Cu-Sn IMCs. The η-phase typically nucleates heterogeneously within 65 ms [59], followed by growth at the interface [60]. At the fast-moving liquid Sn/Cu interface, η-phase IMCs often adopt a scalloped morphology. The morphology and growth kinetics of these scallops vary depending on the crystallographic orientation of the Cu substrate, with distinct differences reported for specific planes [23].

The top-view images in Fig. 9 and Fig. 10 reveal that η-phase grains nucleate randomly on the polycrystalline Cu substrate. Experimental evidence from this study suggests a crystallographic relationship between η-phase grains and the commercial Cu-coated FR4 substrate of approximately $<01\bar{1}0>//<233>$. This relationship implies an angular misalignment of ~10° between the {233} plane of the cubic Cu substrate and the {111} plane of Cu. While prior studies using Cu single crystals have shown specific orientation relationships, such as $\{10\bar{1}0\}/$

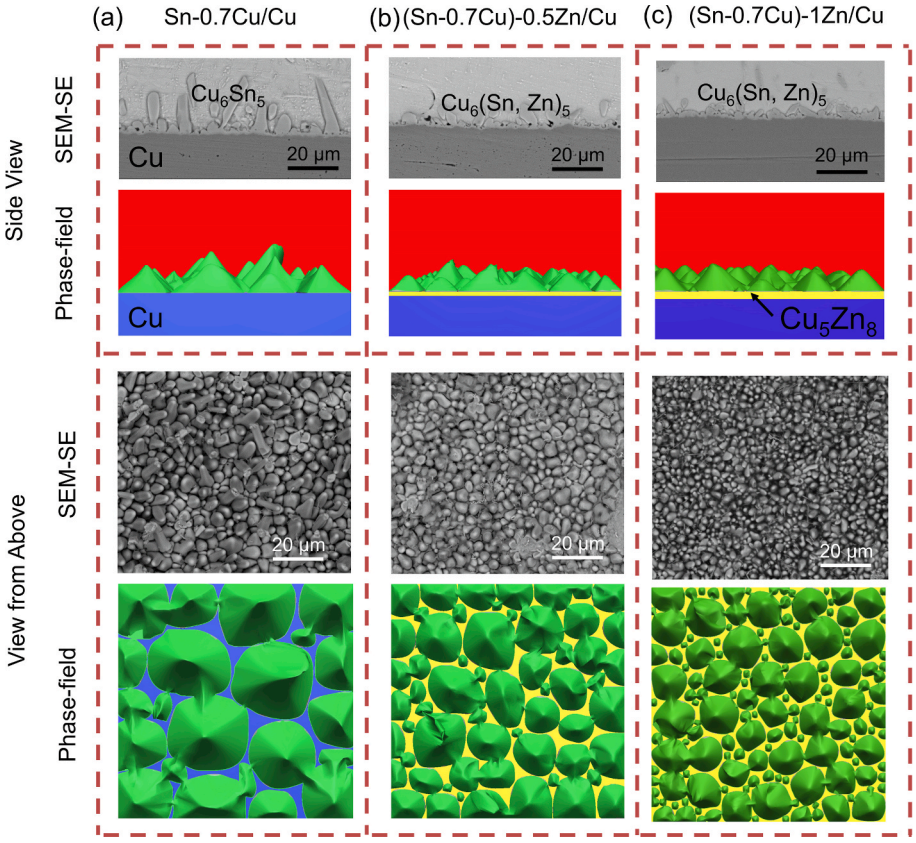


**Fig. 9.** Comparison of experimental and phase-field simulation results for interfacial IMCs from side view and top view. (a) Sn-0.7Cu/Cu, (b) (Sn-0.7Cu)-0.5Zn/Cu, and (c) (Sn-0.7Cu)-1.0Zn/Cu systems in reflowed condition. Phase-field simulation results confirm the experimental observations, showing the formation of a γ-$Cu_5Zn_8$ IMC layer at the Cu interface and an increase in η-$Cu_6Sn_5$ IMC particle density in the Zn-containing solder. Note that IMCs results have been non-dimensionalised for the mathematical convenience.

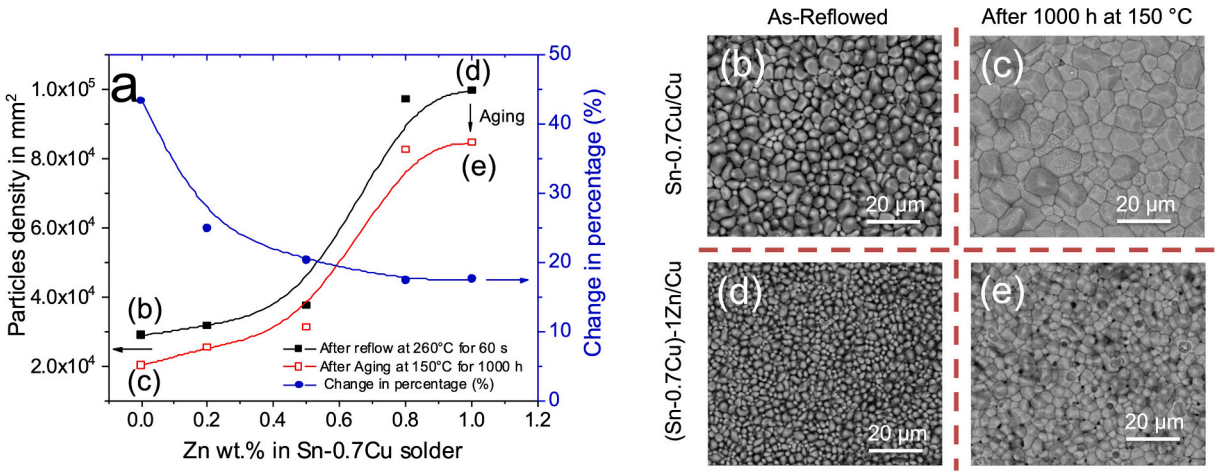


**Fig. 10.** (a) Particle density after reflow and aging at 150 °C for 1000 h, showing the change in the percentage of interfacial IMCs with respect to Zn concentration in the Sn-0.7Cu solder alloy. (b to e) SEM images of η-$Cu_6Sn_5$ IMC particles viewed from above before and after aging for Sn-0.7Cu/Cu and (Sn-0.7Cu)-1.0Zn/Cu systems.

/{111} and {11$\bar{2}$0}//{001} [61], polycrystalline substrates offer insufficient time for preferred orientation development, resulting in random nucleation.

The experimental and phase-field results presented in this work (Fig. 9) highlight the role of the interfacial γ-IMC layer in promoting η-phase nucleation. The presence of this γ-IMC layer at the Cu interface enhances the nucleation potency of the η-phase, leading to significant refinement of η grains. Both the simulation and experimental data confirm this refinement effect. The γ-IMC layer also likely inhibits Cu diffusion into the Sn solder, constraining η grain growth. This inhibition is attributed to the strong chemical affinity between Zn and Cu, which forms a stable γ-phase that acts as a diffusion barrier. The findings emphasise the importance of the γ-IMC layer in controlling interfacial IMC growth and morphology.

This investigation suggests that nucleation and growth of different IMC phases operate simultaneously during the reaction temperatures investigated. Initially, during reflow, the rapid dissolution of Cu into the liquid solder provides an abundant Cu supply, enabling the quick growth of the η-phase IMC layer. In Sn-0.7Cu solder systems, the η-phase forms first, followed by the development of the ε-IMC layer. In contrast, the (Sn-0.7Cu)-xZn/Cu system generates a multi-layered structure comprising η, ε, and γ-IMCs. Once the Cu substrate becomes covered with an IMC layer, Cu diffusion through the IMC layer and along grain boundaries becomes the dominant mechanism for further IMC formation. Grain boundaries and phase boundaries act as high-diffusivity pathways, with diffusion along these paths occurring much faster than lattice diffusion.

The η-phase grain size in reflow reaction follows $t^{1/3}$ growth kinetics akin to Ostwald ripening, rather than the general diffusion-controlled parabolic $t^{1/2}$ kinetics observed for the overall IMC layer growth [43]. The scalloped morphology of the η-phase observed experimentally, with curved grain boundaries and interfaces, aligns with models that incorporate rapid grain boundary diffusion as the primary mass transport mechanism. This emphasises the critical role of grain boundary diffusion in shaping IMC growth during the early stages of soldering.

The presence of intermediate IMC layers, such as ε or γ, significantly affects the growth dynamics of the interfacial η-phase. These layers act as barriers, slowing Cu diffusion to the η-phase, thus impeding its growth. The γ-IMC layer, in particular, hinders rapid mass flux along η grain boundaries, altering the growth and coarsening kinetics of the η-phase. Experimental results (Fig. 10) confirm that η grains undergo coarsening during solid-state reactions, with an increase in average grain size over time reflecting the grain growth kinetics. The scalloped morphology of η-IMCs involves growth at the expense of neighbouring grains, characteristic of a ripening process. However, in the presence of Zn, the coarsening of η grains is significantly suppressed, as evidenced by both experimental and simulation data.

The addition of Zn to the solder alloy introduces further complexities to the diffusion process. Zn reduces Cu and Sn diffusion by forming the γ-phase layer at the solder-substrate interface, which acts as a barrier at the interface and between η-phase grains. This reduces the driving force for coarsening, resulting in a growth mode where grains developed vertically with minimal lateral coarsening. In contrast, systems without Zn experience enhanced Cu flux through grain boundary and triple junctions, which promotes horizontal growth of η grains until neighbouring grains meet. This leads to more significant coarsening during solid-state aging. Consequently, the addition of Zn not only refines the η-phase grain structure but also modifies the growth dynamics, favouring a more stable and less coarsened microstructure.

Following the nucleation and growth of the η-phase, the ε-phase emerges as the second IMC in the Sn-0.7Cu/Cu system. Our experimental analysis revealed a distinct two-layered structure of ε-phase grains (Fig. 7(a)). The first layer comprises columnar ε grains, oriented perpendicular to the Cu substrate. This columnar morphology likely originates from the steep temperature gradient during reflow, which directs heat transfer and facilitates anisotropic growth from the Cu substrate. The second layer features equiaxed ε-phase grains, which nucleate between the columnar grains and the Cu substrate.

During solid-state aging, additional ε grains nucleate and grow, forming new equiaxed ε layers at the Cu/ε and ε/η interfaces, as observed in Fig. 8(a). This behaviour is governed by the diffusion of reactive species, particularly Cu and Sn, and the reaction pathways available. Notably, ε-phase growth is significantly more pronounced in the Sn-0.7Cu/Cu system compared to the (Sn–0.7Cu)-xZn/Cu system. This disparity arises from differences in the supply of Cu and Sn, which diffuse via solid-state mechanisms. At 150 °C, the diffusion rate of Cu in the ε-phase is approximately three times that of Sn in the same phase [62]. For Sn atoms to contribute to the reaction, they must diffuse through the preexisting η and ε layers to reach the Cu/ε interface. In the Sn-0.7Cu/Cu system, the initial layer of columnar ε grains facilitates this diffusion by providing efficient channels for Sn transport. Consequently, new ε grains preferentially nucleate and grow at the triple junctions of columnar grain boundaries and the Cu/ε interface, a phenomenon also noted in prior studies [63].

In contrast, the presence of Zn in the (Sn-0.7Cu)-xZn/Cu system alters this dynamic. The γ-IMC layer, positioned between the Cu substrate and the ε-IMC, serves as a significant diffusion barrier. This layer reduces the rate of Cu diffusion, while the absence or limited number of

columnar ε grains restricts the channels available for Sn diffusion. As a result, ε-IMC growth in the Zn-containing solder is substantially hindered.

The presence of the γ-IMC layer in Zn-containing solder systems has emerged as a critical factor influencing microstructural evolution and interfacial reactions in solder joints. This phase nucleates heterogeneously at the Cu substrate, primarily forming within the Cu-Zn diffusion region before coalescing into a continuous layer. Thermodynamically, the formation of the γ-IMC is highly preferable [56], with a favourable change in the Gibbs free energy of –12.34 kJ/mol, compared to that for the η-phase (–7.42 kJ/mol) [64]. This lower energy threshold and the Zn concentration above a critical threshold during soldering enable the early-stage formation of the γ-phase. Experimental results (Fig. 7(d)) confirm the layer's growth through a diffusion-controlled mechanism, with its thickness increasing notably during prolonged aging.

The γ-IMC layer acts as a diffusion barrier, reducing interfacial reactions that otherwise promote ε-phase growth. Its presence alters diffusion kinetics, decreasing Sn and Cu transport to the ε-phase. This reduction is particularly effective in Zn-containing solders with $\geq$ 0.8 wt % Zn, where ε-phase growth is suppressed, and Kirkendall voids are significantly reduced. These findings demonstrate that Zn's role extends beyond simply forming an additional IMC layer. Due to its affinity for Cu, introduction of Zn allows the formation of γ-IMC layer, in preference to the Cu-Sn IMCs, at the interface between the solder and the Cu-substrate. This is observed in the experimental results and confirmed through the phase-field simulations which indicate formation of this continuous interlayer at the substrate surface. This γ-IMC layer fundamentally alters the growth kinetics of the Cn-Sn IMCs (the η and the ε phases) by absorbing the Cu atoms and altering the diffusion pathways of Cu and Sn atoms, effectively acting as a diffusion barrier. This modification reduces the flux of Cu-atoms required for the growth the η and ε phases, thereby slowing their growth and coarsening during subsequent aging. Phase-field simulations in this study provide crucial mechanistic insights into these processes by visualising when and where the γ-layer forms and its dependence on the Zn concentration. This helps explain the observed growth inhibition of the Cu-Sn IMCs in the Zn containing solder due to the presence of the interfacial γ-layer, offering predictive understanding of Zn's inhibitory effects on IMC formation and growth. Experimental observations (Fig. 5(a) and Fig. 7(b)) highlight that voids are fully interconnected in (Sn-0.7Cu)/Cu systems, resembling line cracks at the interface, whereas Zn-containing systems exhibit fewer and smaller voids (93–325 nm). The presence of Zn not only reduces void formation but also delays crack formation even in solders with intermediate Zn concentrations (e.g., 0.2–0.5 wt%).

Three key findings emerge from the detailed analysis of void formation and interfacial reactions:

(1) **Crack formation in Sn-0.7Cu/Cu systems:** Kirkendall voids form extensively in the ε-phase and often connect, creating a crack at the Cu/ε interface (Fig. 5(a)). These voids are primarily driven by unbalanced Cu and Sn diffusion during aging.
(2) **Suppression of voids in Zn-containing systems:** With Zn concentrations $\geq$ 0.8 wt%, voids are minimised, appearing only sporadically within the ε-phase and remaining isolated, which mitigates structural degradation (Figs. 5(b), (c)).
(3) **Localised reaction and coarsening:** In systems with large voids at the Cu/ε interface, Cu flux to the η-phase diminishes, leading to localised ε-to-η conversion and accelerated coarsening of η grains (Fig. 10(a)).

The reduction in Kirkendall voids in Zn-containing systems is further attributed to Zn's ability to scavenge sulfur from the Cu substrate. Sulfur removal minimises sulfide formation, which has been linked to void initiation and propagation [33,65,66]. This dual role of Zn-forming the γ-IMC layer and scavenging impurities, enhances the integrity of the solder joint.

Fig. 11 provides a schematic representation of the diffusion pathways for Cu and Sn during liquid-state soldering and solid-state aging. The diagrams illustrate the contrasting reaction scenarios with and without Zn. In the Sn-0.7Cu system, the η and ε phases nucleate and grow, accompanied by the formation of Kirkendall voids during aging. In Zn-containing solders, the γ-IMC layer forms in the liquid state, subsequently facilitating η-phase nucleation while suppressing η-phase coarsening, ε-phase growth and void formation. This behaviour emphasises the significance of Zn concentration in optimising solder microstructure and mitigating interfacial degradation mechanisms.

While the benefits are notable, Zn also poses significant drawbacks to solder joints, notably regarding wettability and corrosion [34,67]. Even a small increase from 0 to 1 wt% Zn can drastically worsen wetting, increasing the contact angle from ~ 28° to 52° due to the formation of stubborn zinc oxides that require aggressive fluxes [34]. These fluxes can be corrosive and leave harmful residues. Moreover, Zn's higher anodic potential compared to tin makes the solder joint more prone to galvanic corrosion, potentially weakening it and causing electrical issues [68]. Additionally, the variation in Zn concentration within the interfacial IMC correlates with the volume of the solder and the area of the substrate, consistent with previous studies on the influence of microalloying elements on IMC formation and growth [12,42]. The incorporation of Zn not only affects the interfacial layer composition but also influences the overall mechanical properties and the stability of the solder joints during thermal aging and under operational conditions.

## 5. Conclusions

In this study, we systematically investigated the impact of Zn on the interfacial IMC phase formation and growth in Sn-0.7 wt% Cu solder on a Cu substrate during both liquid and solid-state reactions. The key findings and contributions of this work are as follows:

- Trace amounts of Zn (0.2–0.8 wt%) significantly reduced undercooling, increased nucleation temperature (~1.5 °C), and lowered the growth temperature (~4 °C) of β-Sn, while modifying the eutectic morphology and promoting the formation of CuZn IMC particles in the interdendritic region. Higher Zn levels ($\geq$1 wt%) still reduced β-Sn nucleation undercooling but formed primary γ-$Cu_5Zn_8$ IMC.
- The γ −$Cu_5Zn_8$ IMC layer was found to enhance the nucleation of η-$Cu_6Sn_5$ IMC, ensuring more uniform and refined particles rather than isolated or segregated formations. This effect was attributed to pronounced and uniform nucleation, and the hindrance of Cu diffusion, which restricted growth.
- During solid-state aging, Zn was observed to suppress the growth of ε-$Cu_3Sn$ IMC and the formation of Kirkendall voids at concentrations $\geq$ 0.8 wt%. Zn also caused an increase in γ-$Cu_5Zn_8$ IMC thickness, which impeded grain boundary diffusion, further suppressing the growth of interfacial IMCs and reducing coarsening of η-$Cu_6Sn_5$ IMC.

This study provides clear insights into the role of Zn in Sn-0.7Cu solder, highlighting the impact of γ-$Cu_5Zn_8$ interfacial IMC on the formation and growth of η-$Cu_6Sn_5$ and ε-$Cu_3Sn$ IMCs, as well as on Kirkendall voids. The findings underscore the potential of Zn to modulate the microstructure and reliability of solder joints. Further controlled experiments are needed to fully rationalize the role of γ-$Cu_5Zn_8$ in IMC nucleation and its broader implications in soldering processes.

## CRediT authorship contribution statement

**H.R. Kotadia:** Writing – original draft, Validation, Investigation, Formal analysis, Conceptualization. **A. Rahnama:** Software, Formal analysis. **F. Tang:** Methodology, Investigation. **J.I. Ahuir-Torres:** Software, Formal analysis. **G. West:** Methodology, Investigation. **A. Das:**

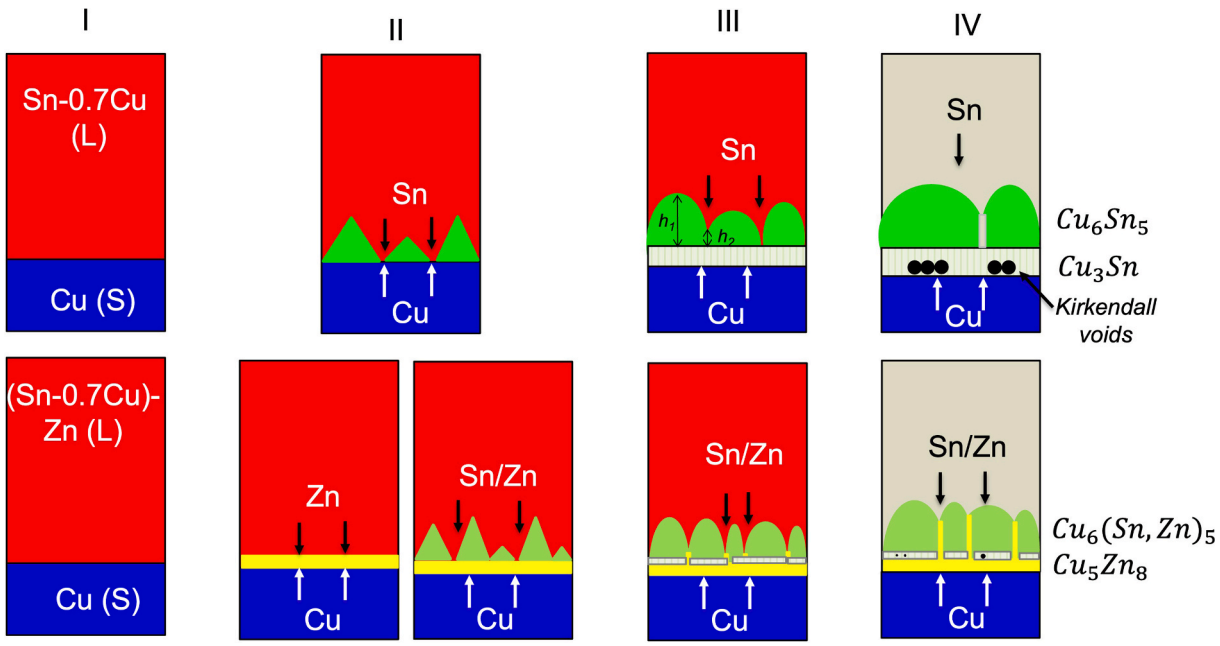


**Fig. 11.** Schematic of reaction scenarios during liquid-state (I–III) and solid-state (IV) interactions between solder and substrate. For Sn-0.7Cu solder, $\eta-\mathbf{Cu_6Sn_5}$ IMC forms during initial melting and fully molten stages (II), thickening by consuming Cu substrate and growing perpendicularly with a prism and subsequently scallop-shaped morphology via grain boundary diffusion. Later, an $\varepsilon-\mathbf{Cu_3Sn}$ IMC layer forms (III), followed by Kirkendall voids during solid-state reactions (IV). In (Sn-0.7Cu)-xZn solder, $\gamma-\mathbf{Cu_5Zn_8}$ IMC (~100 nm) forms first, promoting $\eta-(\mathbf{Cu},\mathbf{Zn})_6$ nucleation while suppressing $\varepsilon-\mathbf{Cu_3Sn}$ and void formation. The $\gamma-\mathbf{Cu_5Zn_8}$ layer reduces Sn and Cu diffusion rates, influencing interfacial reaction kinetics and void mitigation.

Writing – review & editing. **S.H. Mannan:** Writing – review & editing, Supervision, Project administration, Formal analysis, Conceptualization.

## Declaration of competing interest

The authors declare that they have no known competing financial interests or personal relationships that could have appeared to influence the work reported in this paper.

## Acknowledgements

This research was funded by the Engineering and Physical Sciences Research Council, Grant no. EP/G054339/1. In addition to that the characterisation facility is supported from the Higher Education Funding Council for England (HEFCE) fund and the WMG Centre High Value Manufacturing Catapult is gratefully acknowledged. XRD measurements were made using equipment provided by the University of Warwick X-ray Diffraction Research Technology Platform (RTP) and were performed by Dr David Walker.

## Data availability

Data will be made available on request.

## References

[1] J. Glazer, Metallurgy of low temperature Pb-free solders for electronic assembly, Int. Mater. Rev. 40 (2) (1995) 65–93.
[2] H.R. Kotadia, P.D. Howes, S.H. Mannan, A review: on the development of low melting temperature Pb-free solders, Microelectron. Reliab. 54 (6) (2014) 1253–1273.
[3] Product Watch Report - European Commission, EUROPEAN COMMISSION (2021).
[4] T. Dele-Afolabi, M. Ansari, M.A. Hanim, A. Oyekanmi, O. Ojo-Kupoluyi, A. Atiqah, Recent advances in Sn-based lead-free solder interconnects for microelectronics packaging: materials and technologies, J. Mater. Res. Technol. 25 (2023) 4231–4263.
[5] S.-J. Zhong, L. Zhang, M.-L. Li, W.-M. Long, F.-J. Wang, Development of lead-free interconnection materials in electronic industry during the past decades: Structure and properties, Mater. Des. 215 (2022) 110439.
[6] S. Choi, S. Lim, M.M.M. Hanifah, P. Matteini, W.Y.W. Yusoff, B. Hwang, An Introductory overview of various typical lead-free solders for TSV technology, Inorganics 13 (3) (2025) 86.
[7] E. Kirkendall, L. Thomassen, C. Upthegrove, Rates of Diffusion of copper and Zinc in Alpha Brass, University of Michigan, 1938.
[8] Y. Wang, Y. Bian, M. Huang, Kirkendall void inhibition through the elimination of diffusivity mismatch assisted by nanocrystalline metal, Acta Mater. 289 (2025) 120938.
[9] S.E. Nebo, E.H. Amalu, D.J. Hughes, Impact of voids on the solder joint integrity and fatigue life of IGBT power module, Power Electron. Devices Compon. 11 (2025) 100098.
[10] L. Xie, H. Lu, Y. Jiao, S. Qiao, Y. Zheng, A. Li, Y. Chen, X. Han, Interfacial diffusion and Kirkendall voids evolution in the Copper-Zinc alloy binary interface revealed by in situ transmission electron microscopy, J. Alloy. Compd. 968 (2023) 172018.
[11] Z.L. Ma, H. Shang, A.A. Daszki, S.A. Belyakov, C.M. Gourlay, Mechanisms of beta-Sn nucleation and microstructure evolution in Sn-Ag-Cu solders containing titanium, J. Alloy. Compd. 777 (2019) 1357–1366.
[12] H.R. Kotadia, A. Panneerselvam, O. Mokhtari, M.A. Green, S.H. Mannan, Massive spalling of Cu-Zn and Cu-Al intermetallic compounds at the interface between solders and Cu substrate during liquid state reaction, J. Appl. Phys. 111 (7) (2012) 074902.
[13] H.R. Kotadia, S.H. Mannan, A. Das, Influence of Zn Concentration on Interfacial Intermetallics during liquid and Solid State Reaction of Hypo and Hypereutectic Sn-Zn Solder Alloys, J. Electron. Mater. 48 (5) (2019) 2731–2736.
[14] T. Ventura, S. Terzi, M. Rappaz, A.K. Dahle, Effects of solidification kinetics on microstructure formation in binary Sn–Cu solder alloys, Acta Mater. 59 (4) (2011) 1651–1658.
[15] T. Laurila, V. Vuorinen, M. Paulasto-Kröckel, Impurity and alloying effects on interfacial reaction layers in Pb-free soldering, Mater. Sci. Eng.: R: Repor. 68 (1) (2010) 1–38.
[16] G. Zeng, S.D. McDonald, Q. Gu, Y. Terada, K. Uesugi, H. Yasuda, K. Nogita, The influence of Ni and Zn additions on microstructure and phase transformations in Sn–0.7Cu/Cu solder joints, Acta Mater. 83 (2015) 357–371.
[17] C.M. Gourlay, K. Nogita, A.K. Dahle, Y. Yamamoto, K. Uesugi, T. Nagira, M. Yoshiya, H. Yasuda, In situ investigation of unidirectional solidification in Sn–0.7Cu and Sn–0.7Cu–0.06Ni, Acta Mater. 59 (10) (2011) 4043–4054.
[18] H. Soliman, A. El-Taher, M. Ragab, K. Mashaly, M. Amin, Optimizing the performance of Sn–Cu alloys via microalloying with Ni and Zn: a study on microstructure, thermal, and mechanical properties, J. Mater. Sci. Mater. Electron. 36 (2) (2025) 134.
[19] X.F. Tan, Q. Gu, M. Bermingham, S.D. McDonald, K. Nogita, Systematic investigation of the effect of Ni concentration in Cu-xNi/Sn couples for high temperature soldering, Acta Mater. 226 (2022) 117661.

[20] H. Hu, Y. Wang, Q. Jia, B. Zhou, R. Liu, L. Ma, G. Zou, F. Guo, Rapid in-situ formation of Cu-Sn full intermetallic compound films and their joint strengthening mechanisms, Mater. Des. 114241 (2025).

[21] M. Ragab, A. El-Taher, M. Amin, K. Mashaly, H. Soliman, Ni/Zn additions in Sn–Cu solder: enhanced elasticity and reliability via intermetallic strengthening, J. Mater. Sci. (2025) 1–20.

[22] J. Wang, Z. Lv, L. Zhang, F. Duan, J. Wang, F. Li, H. Chen, M. Li, Nucleation and growth of Cu6Sn5 during the aging process of Cu/Sn interface in electronic packaging-by in-situ TEM, Acta Mater. 264 (2024) 119581.

[23] H.F. Zou, H.J. Yang, Z.F. Zhang, Morphologies, orientation relationships and evolution of Cu6Sn5 grains formed between molten Sn and Cu single crystals, Acta Mater. 56 (11) (2008) 2649–2662.

[24] S. Li, X. Wang, M. Liao, Z. Li, Q. Li, H. Yan, A. Liu, F. Wang, Microstructures, mechanical properties and reliability induced from size effect in Sn-based solder joints, J. Mater. Res. Technol. 35 (2025) 5067–5083.

[25] K. Nogita, C.M. Gourlay, S.D. McDonald, Y.Q. Wu, J. Read, Q.F. Gu, Kinetics of the η–η′ transformation in Cu6Sn5, Scr. Mater. 65 (10) (2011) 922–925.

[26] K. Nogita, D. Mu, S.D. McDonald, J. Read, Y.Q. Wu, Effect of Ni on phase stability and thermal expansion of Cu6−xNixSn5 (X = 0, 0.5, 1, 1.5 and 2), Intermetallics 26 (2012) 78–85.

[27] C.-Y. Yu, J.-G. Duh, Stabilization of hexagonal Cu6(Sn,Zn)5 by minor Zn doping of Sn-based solder joints, Scr. Mater. 65 (9) (2011) 783–786.

[28] K. Nogita, C.M. Gourlay, T. Nishimura, Cracking and phase stability in reaction layers between Sn-Cu-Ni solders and Cu substrates, JOM 61 (6) (2009) 45–51.

[29] G. Zeng, S.D. McDonald, Q. Gu, S. Suenaga, Y. Zhang, J. Chen, K. Nogita, Phase stability and thermal expansion behavior of Cu6Sn5 intermetallics doped with Zn, Au and In, Intermetallics 43 (2013) 85–98.

[30] B. Li, A. Yang, M. Peng, Y. Duan, Exploring Zn doped η′-Cu6Sn5: Structural stability, fracture toughness and thermal conductivity, Int. J. Quantum Chem. 123 (14) (2023) e27118.

[31] H.R. Kotadia, O. Mokhtari, M. Bottrill, M.P. Clode, M.A. Green, S.H. Mannan, Reactions of Sn-3.5Ag-based solders containing Zn and Al additions on Cu and Ni (P) substrates, J. Electron. Mater. 39 (12) (2010) 2720–2731.

[32] W.-Y. Chen, C.-Y. Yu, J.-G. Duh, Suppressing the growth of interfacial Cu–Sn intermetallic compounds in the Sn–3.0Ag–0.5Cu–0.1Ni/Cu–15Zn solder joint during thermal aging, J. Mater. Sci. 47 (9) (2012) 4012–4018.

[33] J.Y. Kim, J. Yu, S.H. Kim, Effects of sulfide-forming element additions on the Kirkendall void formation and drop impact reliability of Cu/Sn–3.5Ag solder joints, Acta Mater. 57 (17) (2009) 5001–5012.

[34] H.R. Kotadia, O. Mokhtari, M.P. Clode, M.A. Green, S.H. Mannan, Intermetallic compound growth suppression at high temperature in SAC solders with Zn addition on Cu and Ni–P substrates, J. Alloy. Compd. 511 (1) (2012) 176–188.

[35] A. Luktuke, A.S.S. Singaravelu, A. Mannodi-Kanakkithodi, N. Chawla, Influence of Indium addition on microstructural and mechanical behavior of Sn solder alloys: Experiments and first principles calculations, Acta Mater. 249 (2023) 118853.

[36] R. González-Parra, O. Novelo-Peralta, G. Lara-Rodríguez, I. Figueroa, A. Barba, M. Hernandez, Influence of alloying elements on microstructure, mechanical properties and corrosion behaviour of hypoeutectic Sn-6.5 wt% Zn-0.5 wt% X (X= Ag, Al, Cu) lead-free solders, J. Mater. Sci. Mater. Electron. 35 (22) (2024) 1539.

[37] J. Li, Y.-A. Shen, H. Tatsumi, H. Kotadia, R. Gao, H. Nishikawa, Effect of copper on interfacial reaction and microstructure of soldering on aluminum substrate, J. Mater. Res. Technol. 37 (2025) 3533–3540.

[38] X. Lv, Z. Wang, Z. Pan, C. Zhang, L. Cao, F. Sun, Y. Liu, Research on the interface structure composite behavior and performance influence of Ni and Cr elements in Sn–Cu–Bi–in solder microstructure, J. Mater. Res. Technol. 36 (2025) 713–726.

[39] B. Gao, X. Meng, E. Guo, H. Liang, Z. Cao, T. Wang, Effects of Ni on the nucleation and growth behavior of Cu6Sn5 in Sn–8.5 Cu alloy: an in situ observation, J. Alloy. Compd. 862 (2021) 158603.

[40] Z. Lian, Y. Chen, C. Zhou, M. Li, Z. Dong, W. Lu, Accelerated discovery of lead-free solder alloys with enhanced creep resistance via complementary machine learning strategy, J. Mater. Res. Technol. 32 (2024) 1256–1267.

[41] A. El-Daly, A. Hammad, Enhancement of creep resistance and thermal behavior of eutectic Sn–Cu lead-free solder alloy by Ag and In-additions, Mater. Des. 40 (2012) 292–298.

[42] H.R. Kotadia, A. Panneerselvam, M.W. Sugden, H. Steen, M. Green, S.H. Mannan, Electronics assembly and high temperature reliability using Sn-3.8Ag-0.7Cu solder paste with Zn additives, IEEE Trans. Compon. Packag. Manuf. Technol. 3 (10) (2013) 1786–1793.

[43] J.-C. Liu, G. Zhang, Z.-H. Wang, J.-S. Ma, K. Suganuma, Thermal property, wettability and interfacial characterization of novel Sn–Zn–Bi–In alloys as low-temperature lead-free solders, Mater. Des. 84 (2015) 331–339.

[44] I. Steinbach, F. Pezzolla, A generalized field method for multiphase transformations using interface fields, Physica D 134 (4) (1999) 385–393.

[45] S. Gyoon Kim, W. Tae Kim, T. Suzuki, M. Ode, Phase-field modeling of eutectic solidification, J. Cryst. Growth 261 (1) (2004) 135–158.

[46] M.S. Park, R. Arróyave, Early stages of intermetallic compound formation and growth during lead-free soldering, Acta Mater. 58 (14) (2010) 4900–4910.

[47] M.S. Park, R. Arróyave, Concurrent nucleation, formation and growth of two intermetallic compounds (Cu6Sn5 and Cu3Sn) during the early stages of lead-free soldering, Acta Mater. 60 (3) (2012) 923–934.

[48] C. Rahal, M. Masmoudi, R. Abdelhedi, R. Sabot, M. Jeannin, M. Bouaziz, P. Refait, Olive leaf extract as natural corrosion inhibitor for pure copper in 0.5 M NaCl solution: a study by voltammetry around OCP, J. Electroanal. Chem. 769 (2016) 53–61.

[49] M. Kowalski, P.J. Spencer, Thermodynamic reevaluation of the Cu-Zn system, J. Phase Equilib. 14 (4) (1993) 432–438.

[50] F. Meydaneri, M. Payveren, B. Saatçi, M. Özdemir, N. Maraşlı, Experimental determination of interfacial energy for solid Zn solution in the Sn-Zn eutectic system, Met. Mater. Int. 18 (1) (2012) 95–104.

[51] Y. Kaygısız, S. Akbulut, Y. Ocak, K. Keşlioğlu, N. Maraşlı, E. Çadırlı, H. Kaya, Experimental determination of solid–solid and solid–liquid interfacial energies of solid ε (CuZn5) in the Zn–Cu alloy, J. Alloy. Compd. 487 (1) (2009) 103–108.

[52] B.-J. Lee, N.M. Hwang, H.M. Lee, Prediction of interface reaction products between Cu and various solder alloys by thermodynamic calculation, Acta Mater. 45 (5) (1997) 1867–1874.

[53] S. Bader, W. Gust, H. Hieber, Rapid formation of intermetallic compounds interdiffusion in the Cu□Sn and Ni□Sn systems, Acta Metall. Mater. 43 (1) (1995) 329–337.

[54] J.-H. Shim, C.-S. Oh, B.-J. Lee, D.N. Lee, Thermodynamic assessment of the Cu-Sn system, Int. J. Mater. Res. 87 (3) (1996) 205–212.

[55] G. Zeng, S.D. McDonald, C.M. Gourlay, K. Uesugi, Y. Terada, H. Yasuda, K. Nogita, Solidification of Sn-0.7Cu-0.15Zn solder: In Situ observation, Metall. Mater. Trans. A 45 (2) (2014) 918–926.

[56] C.-Y. Chou, S.-W. Chen, Phase equilibria of the Sn–Zn–Cu ternary system, Acta Mater. 54 (9) (2006) 2393–2400.

[57] J.W. Xian, Z.L. Ma, S.A. Belyakov, M. Ollivier, C.M. Gourlay, Nucleation of tin on the Cu6Sn5 layer in electronic interconnections, Acta Mater. 123 (2017) 404–415.

[58] D. Swenson, The effects of suppressed beta tin nucleation on the microstructural evolution of lead-free solder joints, Lead-free Electronic Solders: a special issue of the Journal of Materials Science: Materials in Electronics, Springer, US, Boston, MA, 2007, pp. 39–54.

[59] O.Y. Liashenko, S. Lay, F. Hodaj, On the initial stages of phase formation at the solid Cu/liquid Sn-based solder interface, Acta Mater. 117 (2016) 216–227.

[60] K.J. Rönkä, F.J.J. van Loo, J.K. Kivilahti, A diffusion-kinetic model for predicting solder/conductor interactions in high density interconnections, Metall. Mater. Trans. A 29 (12) (1998) 2951–2956.

[61] Z.H. Zhang, M.Y. Li, Z.Q. Liu, S.H. Yang, Growth characteristics and formation mechanisms of Cu6Sn5 phase at the liquid-Sn0.7Cu/(111)Cu and liquid-Sn0.7Cu/(001)Cu joint interfaces, Acta Mater. 104 (2016) 1–8.

[62] V. Vuorinen, T. Laurila, T. Mattila, E. Heikinheimo, J.K. Kivilahti, Solid-State Reactions between Cu(Ni) Alloys and Sn, J. Electron. Mater. 36 (10) (2007) 1355–1362.

[63] P.J. Shang, Z.Q. Liu, D.X. Li, J.K. Shang, Directional growth of Cu3Sn at the reactive interface between eutectic SnBi solder and (100) single crystal Cu, Scr. Mater. 59 (3) (2008) 317–320.

[64] C.-C. Pan, K.-L. Lin, The interfacial amorphous double layer and the homogeneous nucleation in reflow of a Sn-Zn solder on Cu substrate, J. Appl. Phys. 109 (10) (2011) 103513.

[65] J. Yu, J.Y. Kim, Effects of residual S on Kirkendall void formation at Cu/Sn–3.5Ag solder joints, Acta Mater. 56 (19) (2008) 5514–5523.

[66] V.A. Baheti, S. Kashyap, P. Kumar, K. Chattopadhyay, A. Paul, Bifurcation of the Kirkendall marker plane and the role of Ni and other impurities on the growth of Kirkendall voids in the Cu–Sn system, Acta Mater. 131 (2017) 260–270.

[67] M.G. Cho, S.-K. Seo, H.M. Lee, Wettability and interfacial reactions of Sn-based Pb-free solders with Cu–xZn alloy under bump metallurgies, J. Alloy. Compd. 474 (1) (2009) 510–516.

[68] Y. Chen, J. Wang, J. Wang, S. Li, F. Tian, H. Chen, G. Peng, M. Li, Corrosion resistance and electrochemical migration behavior of InSnBiAgxZn low-melting-point alloy solders, J. Mater. Res. Technol. 32 (2024) 792–801.